nature communications

Article

https://doi.org/10.1038/s41467-025-62765-z

High-throughput investigation of cyclin docking interactions reveals the complexity of motif binding determinants

Received: 7 March 2025

Accepted: 30 July 2025

Mihkel Örd[1,2], **Matthew J. Winters**[3], **Mythili S. Subbanna**[3], **Natàlia de Martín Garrido**[2], **Victoria I. Cushing**[2], **Johanna Kliche**[4,5], **Caroline Benz**[4], **Ylva Ivarsson**[4], **Basil J. Greber**[2], **Peter M. Pryciak**[3] ✉ & **Norman E. Davey**[2] ✉

Many regulatory protein-protein interactions depend on Short Linear Motifs (SLiMs). In the cell cycle, cyclin-CDKs recognize SLiMs to control substrate recruitment and phosphorylation timing. Here, we measure the relative binding strength of ~100,000 peptides to 11 human cyclins from five families (D, E, A, B, and F). Using a quantitative intracellular binding assay and large-scale tiled peptide screening, we identify multiple non-canonical binders unveiling a broader repertoire of cyclin docking motif types. Cryo-electron microscopy and saturation mutagenesis studies reveal distinct binding modes and sequence features governing motif recognition, binding strength, and cyclin preference. Docking motifs vary from highly selective to pan-cyclin, thereby fine-tuning the timing of CDK phosphorylation during cell cycle. Overall, these findings provide insights into the rules encoding specificity and affinity of SLiM-mediated interactions and offer a framework for understanding motif-driven protein networks across the proteome.

Short linear motifs (SLiMs) play central roles in cellular signaling and regulation by mediating dynamic, transient protein-protein interactions. The human proteome is predicted to contain over 100,000 SLiMs, grouped into >350 classes, each typically consisting of a short (3–10 residue) disordered sequence that binds to a structured domain in a partner protein[1,2]. Many SLiM-binding domains recognize similar motifs in multiple different proteins. Conversely, many homologous domains recognize the same class of motif. This raises fundamental questions about the extent to which individual motifs differ in their binding strength or their domain specificity, and how these differences affect biological outputs.

These questions are exemplified by cyclins, the substrate recruitment subunits of the cyclin-dependent kinases (CDKs) that control division in eukaryotic cells. Cell division requires precise coordination of diverse molecular processes, such as DNA replication, chromosome segregation, centrosome duplication, and transcription[3]. CDKs orchestrate each step by phosphorylating hundreds of proteins in a temporally resolved manner that involves waves of cyclin expression[4–7]. In metazoan cell cycles, four major classes of cyclin-CDK complexes are activated sequentially, with cyclin D-Cdk4/6 and E-Cdk2 initiating cell cycle entry, cyclin A-Cdk1/2 driving S phase and mitotic entry, and cyclin B-Cdk1 coordinating mitosis[8]. The functional diversification of these complexes can arise from differences in their phosphorylation targets. Cyclin subunits are known to recruit phosphorylation targets by binding to docking motifs[9]. In particular, "RxL" docking motifs are recognized by a pocket called the hydrophobic patch that is conserved throughout cell cycle cyclins (D, E, A, B)[10,11]. In CDK substrates, RxL motifs enhance phosphorylation, whereas in CDK

---

[1]University of Cambridge, CRUK Cambridge Institute, Cambridge, UK. [2]The Institute of Cancer Research, Chester Beatty Laboratories, London, UK. [3]Department of Biochemistry and Molecular Biotechnology, University of Massachusetts Chan Medical School, Worcester, MA, USA. [4]Department of Chemistry - BMC, Uppsala University, Husargatan 3, Uppsala, Sweden. [5]Present address: Cell Signaling and Cell Cycle, Danish Cancer Institute, Strandboulevarden 49, 2100 Copenhagen, Denmark. ✉e-mail: peter.pryciak@umassmed.edu; norman.davey@icr.ac.uk

inhibitors they block substrate recognition[12,13] (Supplementary Fig. 1a). Moreover, these interactions can control cyclin localization[14–16]. Cyclin F recognizes RxL motifs but does not bind CDKs, acting instead as a substrate recognition subunit of the SCF (Skp1–Cul1–F-box protein) ubiquitin ligase complex[17]. Additionally, cyclin D docks to C-terminal helices in Rb-family proteins[18], and cyclin B binds to a helix in Mad1 and a phosphoserine-containing motif in separase[19–21]. Further diversity of cyclin docking exists in budding yeast, where specific docking motifs have been found for most cyclin types[22–26].

Over 30 human proteins are known to recruit cyclins through RxL motifs. These motifs generally conform to a strict consensus where an invariant leucine (P0, which we refer to as Φ_0) is flanked N-terminally by an arginine or lysine residue (P-2) and C-terminally by a phenylalanine or a leucine (at P + 1 or P + 2, which we refer to as Φ_C) (Fig. 1a, b). Co-crystal structures of cyclin A2 with RxL peptides[27–29] reveal that the peptide N-terminus including the consensus basic residue makes extensive contacts with the cyclin surface, while the Φ_0 and Φ_C residues are buried in hydrophobic pockets (Fig. 1c). Distinct backbone conformations permit Φ_C to exist at either P + 1 or P + 2. Despite these insights, important questions remain. Notably, human cyclin residues that contact the RxL motif exhibit sequence diversity, particularly those contacting the N-terminal portion of the motif (Fig. 1d), yet it is unclear if different cyclins show distinct motif sequence preferences. In addition, little is known about which residues are tolerated in RxL motifs, how the motif sequence context can modulate binding strength, and whether differences in motif affinity or cyclin specificity can control the timing of CDK substrate phosphorylation. Furthermore, the identification of some atypical, RxL-like motifs[17,30–32], suggests that the full spectrum of potential cyclin-binding peptides remains poorly defined. Given the critical role of cyclin-CDKs in cell proliferation and the considerable interest in inhibiting these complexes for therapeutic purposes[33,34], a systematic effort to address these questions is warranted.

Here, we present a comprehensive investigation of docking interactions across five major human cyclin families, involving over one million quantitative measurements of cyclin-motif binding strength. We identify ~100 previously unreported cyclin-binding peptides and uncover extensive diversity in affinity, specificity, motif types, and binding modes. Our findings define the motif binding determinants for 11 cyclins and describe how sequence variations tune both affinity and cyclin specificity, thereby illuminating how CDK substrate choice can vary during cell cycle progression. This work elucidates the rules governing substrate recruitment by human cyclin-CDKs, while providing broader insights into the principles governing motif-mediated interactions.

Results

SIMBA enables identification of cyclin binding peptides

We applied Systematic Intracellular Motif Binding Analysis (SIMBA), a quantitative yeast-based peptide binding assay[35], to investigate human cyclin docking interactions. In yeast (*Saccharomyces cerevisiae)*, mating and cell cycle are opposing pathways, with yeast Cln2-Cdc28 phosphorylating and inactivating mating pathway proteins[36] (Fig. 1e). In SIMBA, this network is rewired such that an exogenous domain-peptide interaction recruits Cln2-Cdc28 to its mating pathway target, Ste20^{Ste5PM} (Fig. 1f). Consequently, mating signaling and growth arrest are suppressed in proportion to the strength of the exogenous docking interaction. To investigate human cyclins (HsCyclins), we fused their cyclin fold domains (disabled for CDK-binding) to Cln2, and inserted their candidate docking motifs into Ste20^{Ste5PM} (Fig. 1f). The HsCyclin (D1, E1, A2, and B1) fusions recognized the native Cln2 LP docking motif and a pan-cyclin RxL motif from PKN2 (Fig. 1g, Supplementary Fig. 1b, c). Importantly, the RxL interaction was abolished by mutating the human cyclin hydrophobic patch (Fig. 1g), confirming that Cln2 does not interact with RxL motifs[22,23]. Furthermore, testing multiple RxL sequences revealed specificity differences among cyclins (Fig. 1h, Supplementary Fig. 1d). These results established that SIMBA could be used to study human cyclin docking.

Design and validation of a tiled cell cycle protein library

To comprehensively characterize the repertoire of human cyclin binding motifs, we designed a high-throughput SIMBA screen. We selected 808 cell-cycle-related proteins as a pool of potential cyclin binders and represented their intrinsically disordered regions (IDRs) as ~90,000 tiled 16-mer peptides, which overlap by 14 amino acids to delineate motif boundaries with 2-residue precision (Fig. 1i). We cloned this tiled library, including control peptides (wild-type and mutated RxL and LP motifs, and STOP-codon-containing peptides) into Ste20^{Ste5PM}, and expressed 11 human cyclins (D1/2/3, E1/2, A1/2, B1/2/3 and F) as Cln2 fusions (Fig. 1i, Supplementary Fig. 1e). We screened the library against each cyclin in competitive growth assays and used deep sequencing to monitor the frequency of peptides over time, from which enrichment scores were calculated. Most peptides displayed similar enrichment scores with and without a human cyclin (Fig. 1j), suggesting no cyclin-specific suppression of growth arrest and therefore no cyclin binding. The scores were strongly correlated across replicate experiments (Supplementary Fig. 1f). Importantly, the control peptides showed four categories of behavior (Fig. 1j, Supplementary Fig. 1g). First, the highest scoring variants in all strains were those containing STOP codons, which truncate the Ste20^{Ste5PM} protein and thereby eliminate mating signaling (Fig. 1j, k). Second, wild-type LP motif peptides were enriched in all strains expressing Cln2 or HsCyclin-Cln2, confirming that all Cln2 fusions were expressed (Fig. 1j, k). Third, non-functional mutant RxL or LP motifs were not enriched in any of the strains (Fig. 1j, k). Fourth, wild-type RxL control peptides were enriched specifically in strains expressing HsCyclin-Cln2 fusion proteins (Fig. 1j, k). To focus exclusively on interactions mediated by the human cyclins, in subsequent analyses we corrected the enrichment scores from the HsCyclin strains by subtracting those in the unfused Cln2 strain to obtain SIMBA scores (Fig. 1l, Supplementary Fig. 1g–j, Supplementary Data 1). These results demonstrate that SIMBA can be scaled to study large peptide libraries.

An expanded census and diversity of cyclin binding peptides

As expected, cyclin-binding peptides in the tiled library were rare, and most library peptides were not enriched in any HsCyclin-Cln2 strain (Fig. 2a, Supplementary Data 1). This is illustrated by results from RBL1, which contains three IDRs covered by 159 peptides (Fig. 2b). While most of these peptides were not enriched in any HsCyclin strain, two regions showed binding, with the dense peptide tiling delineating motif boundaries with 2-residue precision (Fig. 2b, c). The first region contains a characterized RxL motif[29,37], covered by five peptides that were enriched in cyclin D1, E1/2, A2, and F strains (Fig. 2b, c). The second region, at the C terminus of RBL1, contains three peptides that were strongly enriched only in cyclin D1/2/3 strains (Fig. 2b) confirming prior findings that this region contains a helical cyclin D-binding motif[18]. This result also demonstrates that the screen can identify peptides for distinct cyclin pockets, as cyclin D-binding helices do not bind to the hydrophobic patch[18]. Thus, combining the high-throughput SIMBA method with the tiled peptide library allows unbiased identification of binding motifs, while simultaneously defining their boundaries and cyclin specificities.

The screen identified 75% (21/28) of the published cyclin binding motifs in the tiled library, demonstrating its ability to capture biologically relevant interactions. In addition, 27 unreported high-confidence motifs were discovered (Fig. 2d, Supplementary Data 2). The number of detected binding regions varied considerably between cyclins, with the highest observed for cyclins F and A2, and lower numbers for D1, E1, and B1 (Fig. 2a, Supplementary Data 2). Cyclins E1, A2, and F bound many of the published RxL motifs but D1 and B1 did not bind strongly to any. However, these cyclins did bind previously uncharacterized RxL motifs including a cyclin D1-binding motif in INSM1, a reported D1 interactor[38], and a strong B1-binding motif in MICAL3 (Fig. 2e, black motifs). The screen also uncovered atypical motifs. MASTL, a key mitotic regulator[39], recognized cyclin B1 via a partial RxL consensus match that lacks a Leu or Phe at the Φ_C position (KNLMCEL) (Fig. 2e). Similarly, cyclin A2 bound an RNLSSEF peptide in GMNC, a DNA replication protein[40], and an unconventional RxLxY peptide in SGO1 (Fig. 2e). Further, cyclin B1 bound two atypical motifs in PKN2: a QxLxF and a TxLxF, the former of which was also detected by Proteomic Peptide Phage Display (ProP-PD) (Fig. 2e, Supplementary Fig. 1b, c). Interestingly, many of these proteins also contained RxL

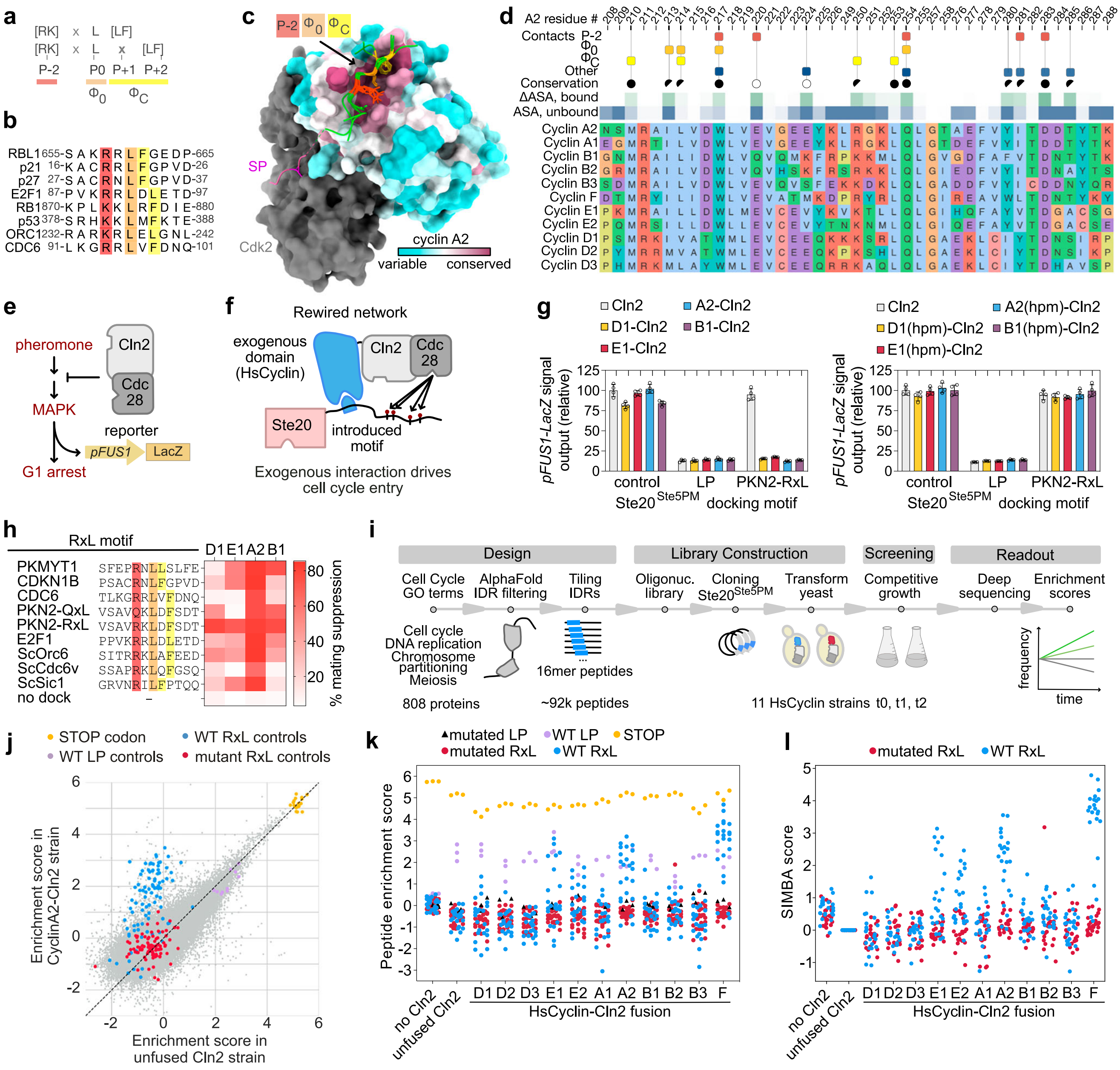

Fig. 1 | Systematic Intracellular Motif Binding Analysis (SIMBA) enables low- and high-throughput cyclin binding peptide characterization. **a** RxL motifs contain a central Leu at position P0 flanked by Arg/Lys at P-2 and Leu/Phe at P + 1 or P + 2. **b** Alignment of structurally characterized RxL peptides. **c** Superimposed structures of human cyclin A2-Cdk2 with RxL peptides bound to the hydrophobic patch and a phosphorylation site (SP) in the enzymatic cleft (PDB: 2CCI, 1H24-28). **d** Alignment of human cyclins showing selected positions that are near the bound RxL peptides. Colored boxes indicate cyclin residues that contact the indicated peptide positions. Conservation symbols denote cyclin positions with no variation (filled circles), variation with similar amino acids (half-circles), and variation with physico-chemically different amino acids (empty circles). ASA, accessible surface area, darker color indicates higher value. **e** Scheme illustrating yeast mating signaling and its inhibition by Cln2-Cdc28. **f** The rewired network in SIMBA, where docking between an introduced motif and a human cyclin fused to Cln2 drives inhibitory phosphorylation of its mating pathway target, a fusion protein called Ste20^{Ste5PM}. The inhibitory effects can be assayed by low-throughput assays (involving a transcriptional reporter, *pFUS1-lacZ*) or high-throughput assays (involving competitive growth). **g** Suppression of mating signal by wild-type and hydrophobic patch mutant (hpm) cyclins measured by a *pFUS1-lacZ* reporter. Ste20^{Ste5PM} harbored a control motif, a Cln2-binding motif (LP), or an RxL motif (PKN2-RxL). Bars, mean ± standard deviation (SD); $n = 4$ biological replicates. **h** Cyclin-motif docking measured by mating suppression relative to unfused Cln2 (mean; $n = 4$). **i** The cell cycle protein peptide tiling SIMBA experiment outline. **j** Enrichment scores of 91k peptide-encoding sequences in SIMBA competitive growth experiments with cyclin A2-Cln2 and unfused Cln2. **k, l** Enrichment scores of control peptides in the tiled library. Plots show raw scores (**k**) or Cln2-corrected enrichment scores (**l**). Source data are provided as a Source Data file and in Supplementary Data 1.

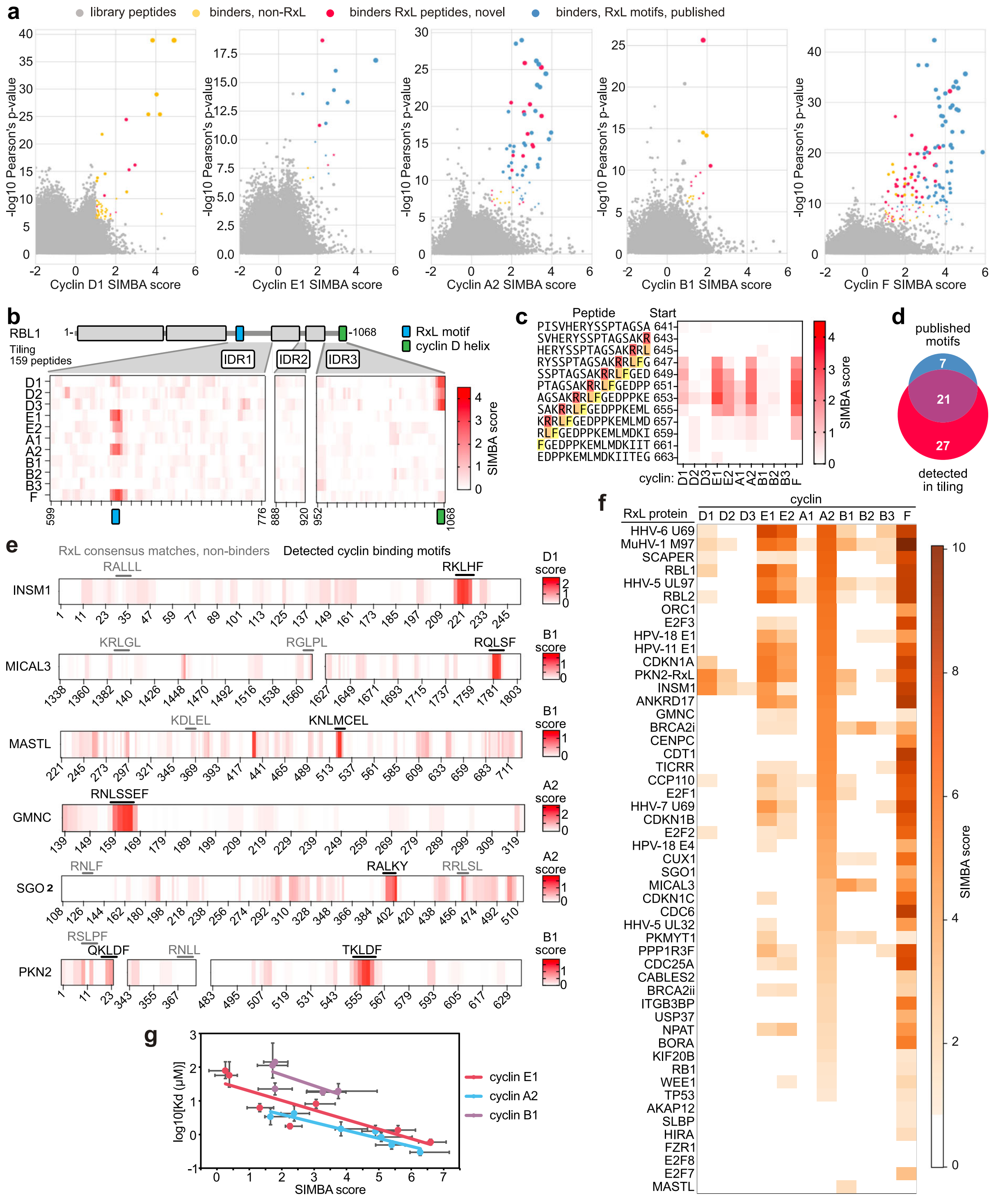

Fig. 2 | Quantitative high-throughput measurements identify cyclin binders and reveal differences in RxL binding affinity and cyclin specificity. **a** Identifying cyclin binders in the tiled library screen. P-values from two two-sided t-tests comparing peptide scores in HsCyclin strain to unfused Cln2 and no Cln2 strains were combined with Pearson's method. Pearson's p-value thresholds were 10^{-10} (high confidence; circles) and 5.5×10^{-7} (low confidence; stars). Symbols are sized by the product of the SIMBA score and the inverse log10 p-value. Control peptides are omitted. **b** SIMBA scores of tiled peptides from the IDRs of RBL1. Results were smoothened by plotting rolling medians of 3 consecutive peptides. **c** SIMBA scores (smoothened) of tiled peptides surrounding the RBL1 RxL motif. **d** 21 out of 28 published docking motifs and 27 unreported motifs were detected as high confidence cyclin interactors. **e** SIMBA scores (smoothened) of tiled peptides from six proteins for the indicated cyclin. RxL motifs that bind are black; non-binding motifs are gray. **f** SIMBA scores of cyclins binding to 51 RxL peptides. For clarity, only scores >1 are shown. **g** Correlation between SIMBA scores (median ± 95% CI; from at least 8 independent measurements) and peptide-cyclin dissociation constants (Kd) measured by competitive FP (mean ± 95% CI; *n* = 2 biological replicates). The Kd values are inferred from IC50 measurements with FITC-PKN2 RxL peptide. For MASTL, the CI could not be calculated. Source data are provided as a Source Data file and in Supplementary Data 1, 2 and 4.

consensus matches that did not bind any cyclin, suggesting that the presence of an RxL consensus alone may not be sufficient to encode a functional RxL motif (Fig. 2e, gray motifs). Altogether, these findings expand the census of cyclin docking motifs in the human proteome, including motif types that deviate from the typical RxL consensus, and show that a consensus match does not ensure binding.

RxL motifs show diverse affinities and cyclin preferences

To directly compare different RxL motifs, we performed SIMBA experiments with a collection of motifs from human and viral proteins, screened as 13-mer peptides centered on the Φ_0 Leu. These motifs varied in both binding strength and cyclin specificity. The strongest binding peptides were generally from viral proteins, although several human peptides showed comparable binding (e.g., SCAPER and RBL1) (Fig. 2f). We identified three major categories of specificity for CDK-binding cyclins (D, E, A, B). First, pan-cyclin peptides, such as those from INSM1 and the viral protein MuHV-1 M97, which bind to members of all four families. Second, partially selective peptides, such as CDKN1A (p21) and RBL1 peptides that bound all cyclin types except B, or peptides from ANKRD17 and HPV-11 E1 that exhibited a more restricted preference for cyclins E and A but not D or B. Third, cyclin-specific peptides, which show strong preference for particular cyclin types. For example, SCAPER, ORC1, CDT1, and CENPC bound preferentially to cyclin A2, while MASTL bound only B-type cyclins. Thus, RxL motifs exhibit a variety of cyclin specificities. To validate the SIMBA findings, we performed competitive fluorescence polarization (FP) assays to measure peptide affinities for purified cyclin-CDK complexes (Supplementary Fig. 2a, b). We tested peptides spanning a broad range of SIMBA scores and found that these in vivo scores correlated well with in vitro binding affinities for each cyclin, although the Kd for a given SIMBA score differed between cyclins (Fig. 2g). These assays also confirmed cyclin preferences, such as cyclin B1's exclusive ability to bind the MASTL peptide and its poor binding to the RBL1 peptide (Supplementary Fig. 2b). Hence, the SIMBA data provide reliable quantification of relative binding strength and specificity, revealing detailed insights into cyclin-CDK recruitment.

RxL binding determinants and unexpected binding modes

To elucidate binding preferences of each cyclin, we conducted a comprehensive mutational interrogation of 51 peptide motifs, including published motifs and previously uncharacterized instances identified either in the SIMBA tiling screen or by ProP-PD. We designed deep mutational scanning (DMS) libraries that included saturation mutagenesis of 22 peptides and alanine scanning of 29 others, and performed SIMBA experiments to screen these mutant variants against 11 human cyclins (Supplementary Data 3–4). As a quality check, we compared 48 control peptides present in both the tiled and mutational scanning libraries and observed high correlation between their scores in the different screens (Supplementary Fig. 3a). Pairwise comparisons of cyclins for their binding to the 7968 peptides in the mutational scanning library revealed the strongest correlation between cyclins E1 and E2, followed by A2 and F, and D1 and D2 (Supplementary Fig. 3b). Notably, cyclin B3 was more similar to E1/2 than B1/2 (Supplementary Fig. 3b).

The impact of alanine mutations across the peptides confirmed the requirement for the three core positions: Arg/Lys at P-2, Leu at Φ_0, and a second Φ_C hydrophobic residue at P + 1 or P + 2 (Fig. 3a, Supplementary Fig. 3c). Surprisingly, we found that two peptides with the sequence RxLL, a published motif from PKMYT1 (RNLLSLF)[41] and one from BRCA2 found in the tiled library (RNLLNEF), did not depend on the Leu at P + 1 and instead required the Phe at P + 4 (Fig. 3a). Furthermore, we observed the same P + 4 requirement in peptides from the tiled library screen (GMNC, MASTL, and CABLES2) that lacked a Leu or Phe at both P + 1 and P + 2 (Fig. 3a, Supplementary Fig. 3c).

Based on these observations, we propose grouping RxL motifs into three types − type 1, type 2, or type 3 − based on whether the required Φ_C hydrophobic residue is at P + 1, P + 2, or P + 4, respectively (Fig. 3a, Supplementary Fig. 3c). The averaged DMS data for each type highlight the strong preferences at the three core positions and confirm that the Φ_C hydrophobic residue can be provided at P + 1, P + 2, or P + 4 (Fig. 3b, Supplementary Fig. 3d, Supplementary Data 5). Interestingly, we found no example of a similar preference at P + 3, suggesting that type 3 motifs bind with a unique backbone conformation. To investigate this further, we used cryo-EM to determine the structure of cyclin A2-Cdk2 bound to the type 3 peptide from GMNC. Indeed, the cyclin-bound peptide forms a single turn α-helix from P0 to P + 4, allowing the Phe at P + 4 to engage the same cyclin pocket contacted by the Φ_C hydrophobic residues in type 1 or 2 peptides (Fig. 3c, d, Supplementary Fig. 4a–g). Thus, the three RxL types allow the core position contacts to be provided by three distinct peptide conformations. The RxL type was not a strict determinant of cyclin specificity, because most cyclins bound motifs of all types, although cyclin E1 preferred type 1 motifs, and cyclin D1 did not detectably bind any type 3 motifs (Fig. 3e). These findings uncovered a distinct motif category that was previously unrecognized.

RxL consensus match is a poor determinant of cyclin binding

Next, we explored the contribution of RxL consensus residues to cyclin binding. The tiled library contained 427 peptides matching the common RxL consensus sequence, ([RK]xLx{0,1}[FL]), including 287 that match a stricter consensus ([^EDWNSG][^D][RK][^D]Lx{0,1}[FL]x{0,3}[EDST]) defined previously[2,42]. We observed cyclin binding to less than 15% of the peptides with the strict consensus (Supplementary Fig. 4h), indicating that most are not cyclin binders. To test how binding depends on the residue identity at each variable consensus position (P-2 and Φ_C), we directly compared all four consensus combinations (RF, RL, KF, KL) in 42 parental peptides (Fig. 3f). Both positions showed clear preferences. At P-2, Arg was preferred over Lys by all cyclins, with the degree of this preference being stronger for cyclins E1 and F than for A2 and B1 (Fig. 3f). At the Φ_C position, Phe was strongly preferred over Leu by all cyclins. This was independent of whether P-2 was Arg or Lys, but it was greater in type 1 motifs compared to type 2 (Fig. 3f). The two positional preferences were additive, such that motifs with favored residues at both positions (RxLF, RxLxF) permitted the strongest binding and the broadest range of cyclins. Conversely, only a minority of KxLxL motifs were binders (favoring cyclins A2 and F) and KxLL motifs were uniformly poor binders. Thus, variation in core residues alone can modulate the binding strength of RxL motifs. Conversely, peptides with optimal cores (RxLF or RxLxF) still vary in binding strength, and hence core residues alone are not sufficient to determine binding.

Non-core positions modulate RxL affinity and specificity

To obtain an overview of motif preferences for all cyclins, we grouped the DMS data by position for each of the three RxL types (Fig. 4a, Supplementary Fig. 5a). This analysis revealed that, in addition to the three core positions, the residues at P-4, P-3, and P-1 are also strong binding determinants. Positions C-terminal to the core play a lesser role but show a preference for acidic residues that is most apparent for D and B cyclins. Compared to types 1 and 2, type 3 motifs tolerate fewer amino acids in most of the non-core positions (see numbered boxes in Fig. 4a).

At P-4, we identified strong preferences for nonpolar side chains (Ala, Val, Ile, Cys) (Fig. 4a, Supplementary Fig. 5a). Moreover, in structures of cyclin-peptide complexes, the P-4 residue is usually buried to a similar extent as the Φ_0 Leu (Supplementary Fig. 5b), supporting a key role for P-4 as a third hydrophobic interaction which we refer to as Φ_N. The residues favored at P-4 are largely shared among cyclins, but there are some differences that contribute to cyclin specificity (Fig. 4a, Supplementary Fig. 5c). For example, cyclins B1 and B2 tolerate Leu and Ile at P-4 while disfavoring Ala, which is the preferred

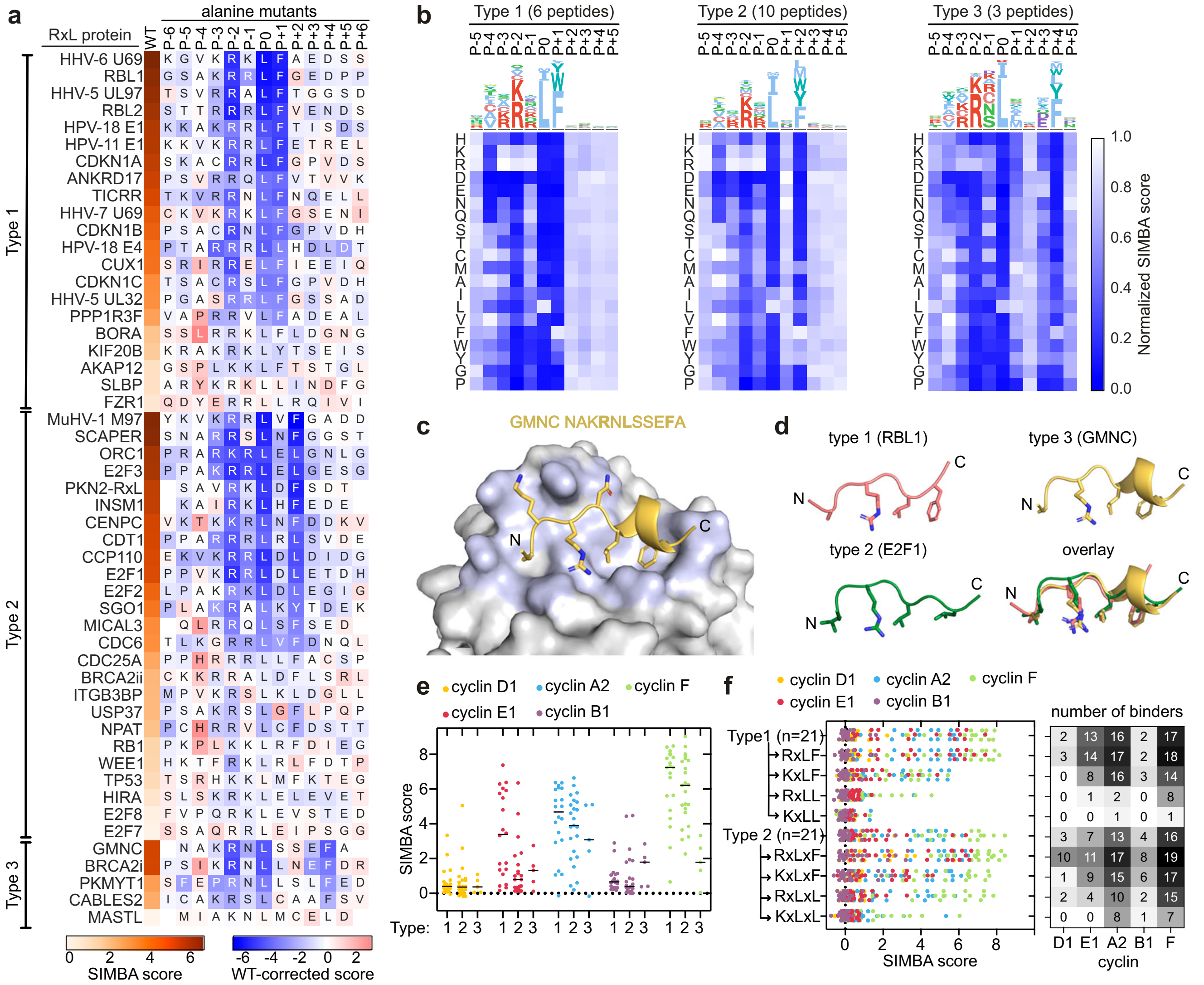

Fig. 3 | Mutational scanning reveals the impact of RxL motif core residues on cyclin binding. **a** RxL peptide alanine-scanning results for cyclin A2. The leftmost column shows wild-type peptide scores. Letters show the peptide sequence, and the color of the box shows the wild-type-corrected score of the peptide with Ala at that position. **b** Sequences logos and heatmaps showing amino acid preferences at different positions of type 1, 2, and 3 RxL motifs for cyclin A2. Data is averaged over multiple peptides subjected to DMS. **c** Cryo-EM structure showing the GMNC RxL peptide binding to the cyclin A2 hydrophobic patch; contact residues from Fig. 1d are shaded light blue. **d** Structures of cyclin-bound type 1 (PDB: 1H28), 2 (PDB: 1H24) and 3 (PDB: 9HIU) peptides. **e** SIMBA scores of natural type 1, 2 and 3 peptides. Lines, median. **f** The impact of having either Arg or Lys at P-2 and Leu or Phe at Φ_C was studied by generating mutants with all combinations in the control RxL peptides. Source data are provided as a Source Data file and in Supplementary Data 5.

residue for cyclin D1. Notably, the cyclin B1/B2-favoring RxL from MICAL3 has Leu at P-4 (Fig. 4b). DMS of this peptide showed that while cyclin B1 prefers Leu, Ile, and Val at P-4, binding to other cyclins was strongly improved by mutating the Leu to many other residues (Fig. 4b, c). Therefore, Leu at P-4 may act as a specificity filter, favoring cyclin B binding. Similarly, the cyclin B1 specific RxL motif from MASTL contains an Ile at P-4, and replacing it with Cys allowed cyclin A2 to bind (Fig. 4d, Supplementary Fig. 5d). Suboptimal residues in the core positions of the MASTL motif might contribute to the specificity-determining effect of the P-4 residue, because cyclin A2 can tolerate Ile or Leu at P-4 in some other motif contexts (Supplementary Fig. 5c).

At P-3, most cyclins prefer Lys, Arg, Val, or Cys, although cyclin D favors small nonpolar residues (Ala, Cys, Ile) and cyclin B1 prefers Val (Fig. 4a). The contribution of P-3 residues to cyclin specificity is evident in data from a BRCA2 motif, where the wild-type peptide with Lys at P-3 binds both cyclin A2 and B1, but mutating P-3 to Ile or Glu increases B1 binding while significantly decreasing A2 binding (Fig. 4e). At position P-1 (the 'x' of RxL), type 1 and 2 motifs prefer Arg, Lys and Gln, whereas type 3 motifs show a unique preference for Asn, Ser and Cys (Fig. 4a), which might stabilize the adjacent helix by acting as an N-cap[43]. Despite similar preferences at P-1 for most cyclins, this position critically impacts cyclin specificity in several motifs. For example, the SCAPER RxL is among the strongest cyclin A2 binders, but binds other cyclins poorly (Fig. 2f). Interestingly, this motif gained the ability to bind cyclins D1 and E1 if the Ser at P-1 was mutated to any of several preferred residues (Fig. 4f, g). Furthermore, cyclin B3 showed an unusual preference for Thr, Ser and Val at P-1 (Supplementary Fig. 5a, e). Thus, despite overlapping preferences, cyclins differ in their tolerance for suboptimal residues, and these differences can function as specificity determinants.

Finally, to verify the impact of non-core positions, we took one peptide of each RxL type and swapped their 4-residue N-terminal flanks with those from 42 different RxL peptides, and observed that these flanks could strongly alter binding strength (Supplementary Fig. 5f). The results highlight the importance of the P-4 residue, in that cyclin D1 favored flanks with Ala at P-4 whereas cyclin B1 favored those

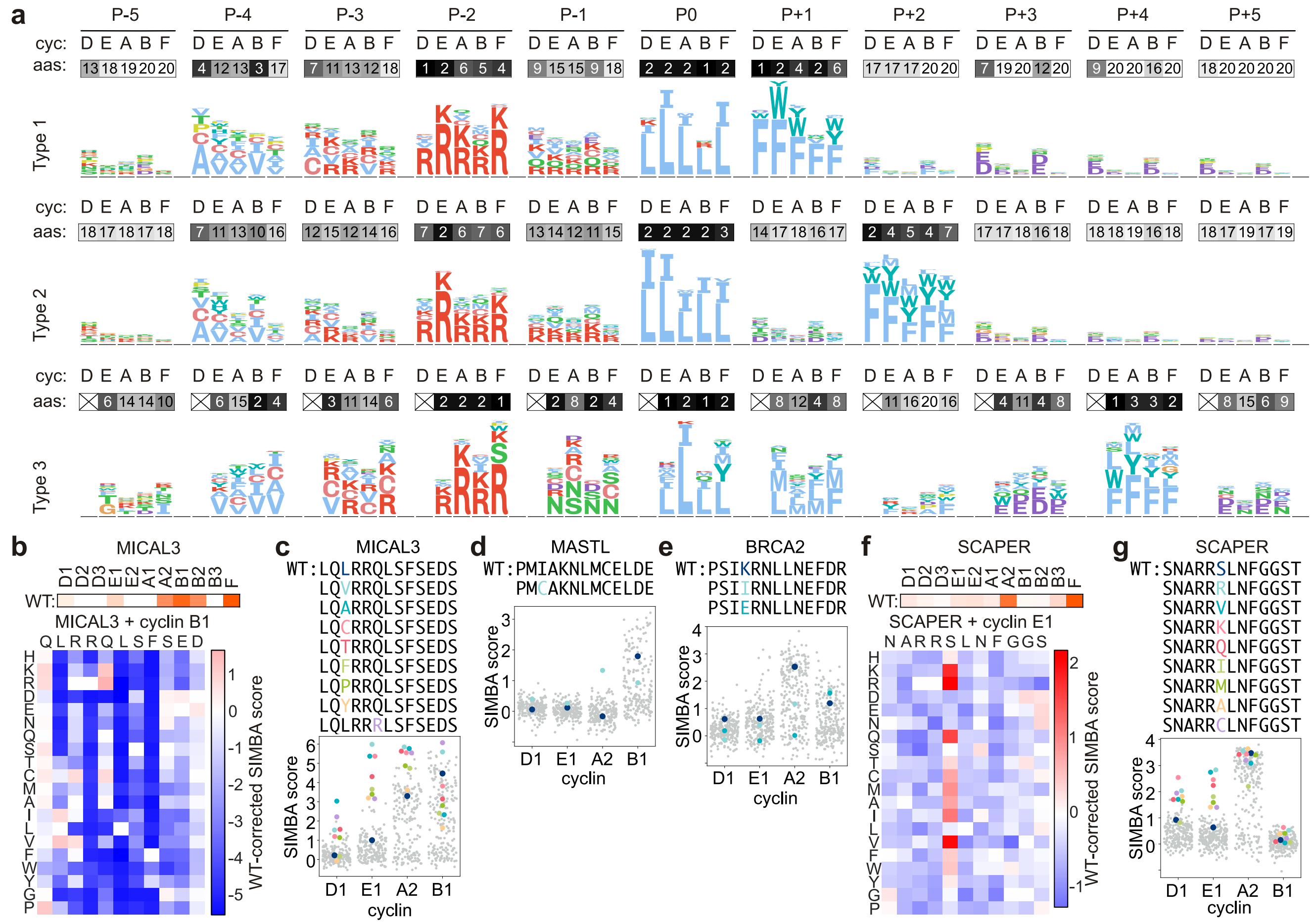

Fig. 4 | Multiple binding determinants modulate cyclin recognition. a Sequence logos showing the favored residues at each position of RxL motifs for cyclins D1, E1, A2, B1 and F. DMS data of peptides where the wild-type bound the cyclin were averaged for each RxL type. Heatmaps show the average number of tolerated amino acids in each position. **b** SIMBA scores of wild-type MICAL3 RxL for each cyclin (top) and its DMS variants for cyclin B1 (bottom). **c**–**e** SIMBA scores of MICAL3 (**c**), MASTL (**d**) and BRCA2 (**e**) DMS peptides. **f** SIMBA scores of SCAPER peptide DMS variants binding to cyclin E1. **g** SIMBA scores of SCAPER peptide DMS variants. Source data are provided in Supplementary Data 4 and 5.

with Val (Supplementary Fig. 5f). Most N-terminal preferences were shared by all 3 RxL types, although some flanks, such as SSLR for cyclin B1, were optimal only in the type 3 context. In analogous experiments at the C-terminal end, we observed much weaker sequence dependence, as most C-terminal flanks were tolerated (Supplementary Fig. 5g). Taken together, the DMS and flank swapping analyses demonstrate that the non-core positions contribute to binding strength and play a key part in determining the cyclin specificity of the motif.

Core and non-core residues collectively tune RxL affinity

Next, we explored the general features controlling affinity. The mutational scanning data revealed that binding strength can be increased for all 51 peptides (Fig. 5a), indicating that none are maximized. Overall, 51% of the mutations in RxL peptides had little to no effect, while 34% reduced binding to all cyclins (D1, E1, A2, B1 and F) and 15% produced cyclin-specific effects (Fig. 5a). This analysis also revealed that peptides with weak core determinants had low tolerance to mutation. For instance, a KxLxL peptide from ORC1 binds strongly to cyclin A2 despite having suboptimal residues at two core positions (Figs. 2f, 3a). DMS of this ORC1 peptide revealed limited tolerance to mutations at P-4, P-3, and P-1, in addition to the three core positions (Fig. 5b). This suggests that the ORC1 peptide tolerates the weak core motif because it has optimal non-core residues. A similar relationship between suboptimal core residues and increased dependence on non-core positions is observed when comparing a wild-type E2F1 motif (RxLxL) to an optimized RxLxF variant (Fig. 5b). Thus, while non-core residues are less essential than core residues, they can enhance binding strength and compensate for suboptimal cores. This concept was supported by binding determinant modeling using DMS data to generate position-specific scoring matrices (PSSMs). These PSSMs allow us to sum the weighted residue preferences at all positions and calculate predicted scores for all natural peptides in our libraries, including additional uncharacterized peptides that contain RxL consensus matches (Fig. 5c, Supplementary Fig. 5h). We observed that, once a threshold was surpassed, there was a strong correlation between predicted and experimental scores (Fig. 5c). We then scored these peptides using a PSSM generated from only non-core residues, and found that these non-core PSSM scores were markedly stronger for binder peptides than non-binders (Fig. 5d). These results explain why most RxL consensus matches are non-binders and emphasize that cyclin binding strength is a cumulative property encoded by preferences at multiple positions along the peptide motif.

Context-specific positioning of the Φ_N residue

Five outlier peptides had substantially stronger binding than predicted by their PSSM scores (Fig. 5c, Φ_N-alt). Interestingly, these peptides contain Pro or Gly at P-3 and a bulky hydrophobic Leu or Phe at P-5 (Supplementary Fig. 5i), which are generally disfavored (Supplementary Fig. 5a). DMS of two such motifs (CDC6 and PKMYT1) revealed a

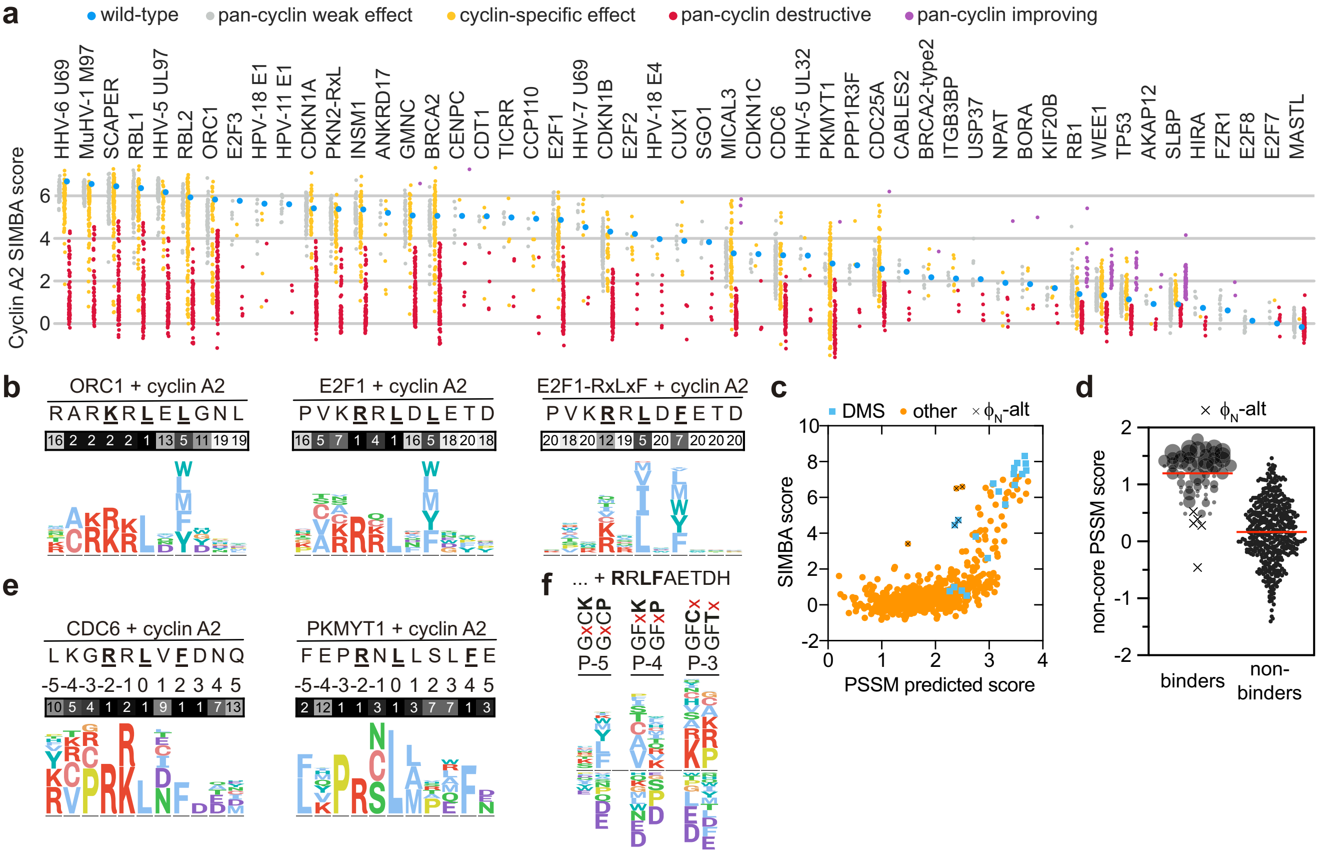

Fig. 5 | Non-core positions play a key role in determining RxL strength and cyclin specificity. a Cyclin A2 SIMBA scores from mutational scanning of 51 peptides. Variants with scores <75% or >125% of the starting peptide were considered destructive or improving, respectively, while variants within that range were considered to have a weak effect. If this change differed by over 50% between cyclins, the effect was considered cyclin-specific. **b** Sequence logos representing DMS data of ORC1, E2F1 and E2F1-RxLxF motifs with cyclin A2. Heatmaps show the number of amino acids tolerated per position. **c** Correlation between PSSM-predicted scores and observed scores of cyclin A2 binding to wild-type RxL peptides. **d** Distributions of PSSM-predicted scores calculated from non-core residues only. Binder symbols are sized proportional to the SIMBA score of the parent peptide. Red lines, median ($n = 65$ binder peptides and 485 non-binder peptides). **e** Sequence logos representing CDC6 and PKMYT1 DMS data with cyclin A2. Heatmaps show the number of amino acids tolerated per position. **f** An E2F1-based RxL motif (RRLFAETDH) was appended with distinct N-terminal sequences and subjected to DMS at the position noted with 'x'. The logos show cyclin A2 preferences at the indicated position. Source data are provided as a Source Data file.

strong preference for Pro at P-3 and a greater dependence on P-5 than seen with other RxL motifs (Fig. 5e). Co-crystal structures with E2F1 (VKRRLDL) and CDC6 (LKGRRLVF) peptides show that the P-4 Val in E2F1 and the P-5 Leu in CDC6 bind the same pocket on cyclin A2[27,29] (Supplementary Fig. 5j). Thus, distinct binding modes could underlie the unusual N-terminal requirements. We probed the interdependence of preferences at P-5, P-4, and P-3 by DMS of these positions in parent peptides differing by a single residue. This revealed that large hydrophobic residues (Leu, Phe, Tyr) were strongly favored at P-5 when P-3 was Pro (Fig. 5f). The presence of Pro at P-3 also reduced the usual P-4 preference for small aliphatic residues and instead imposed a weak preference for basic residues (Fig. 5f). At P-3, Pro or Gly were favored when a Phe at P-5 was the sole hydrophobic residue but not when a Cys was available at P-4 (Fig. 5f). Thus, the N-terminal preferences are contingent upon the available Φ_N residue. The flexible positioning of the Φ_N residue is comparable to that of the Φ_C residue, as both allow key pocket interactions to be encoded at multiple sites within the peptide via distinct backbone conformations, which then impose unique constraints on adjacent positions.

Atypical RxL-like motifs lacking P-2 basic residues

While most cyclin binding motifs detected in the tiled library conformed to the classical RxL consensus (Fig. 2a, Supplementary Data 2), several hits were only partial matches. The first category lacks a basic residue at P-2. For example, the cyclin A2-specific peptide from SAMHD1 contains an LF sequence but has a Val at P-2 (Fig. 6a). Despite this, the SAMHD1 peptide bound cyclin A2 with an affinity comparable to many typical RxL peptides (Supplementary Fig. 6a, b). DMS of this SAMHD1 peptide showed that binding to cyclin A2 has an absolute requirement for the LF sequence plus distinct preferences from P-5 to P-1 (Fig. 6a). The interaction was improved by mutating the P-2 Val to Arg or Lys, which creates an RxL consensus ([RK]QLF), yet for several cyclins binding was improved to a similar or greater degree by mutations at P-4 (Fig. 6b). This suggests that similar atypical RxL-like motifs could also be strong interactors of other cyclins and can be tighter binders than many typical RxL motifs. Interestingly, the preferred residues at P-4 for the SAMHD1 motif are similar to those of typical RxL motifs (i.e., Cys, Ala, and Val), suggesting similar binding topologies, whereas P-5 and P-3 are more restrictive, perhaps to compensate for the lack of Arg/Lys at P-2 (Figs. 3b, 6a). Using cryo-EM, we determined that the hydrophobic core (LF) of the SAMHD1 peptide contacts the cyclin A2 hydrophobic patch in a similar manner as consensus RxL motifs, and that the strongly preferred basic residues at P-5 and P-3 bind to acidic pockets distinct from the usual P-2 contacts (Fig. 6a, c, Supplementary Fig. 6c–h). We found a cyclin A2-binding SQLF peptide from CDAN1 via phage display screening that also bound exclusively to cyclin A2 in SIMBA experiments (Fig. 6d). As with SAMHD1, alanine scanning of this CDAN1 peptide showed a key role for a P-3 basic

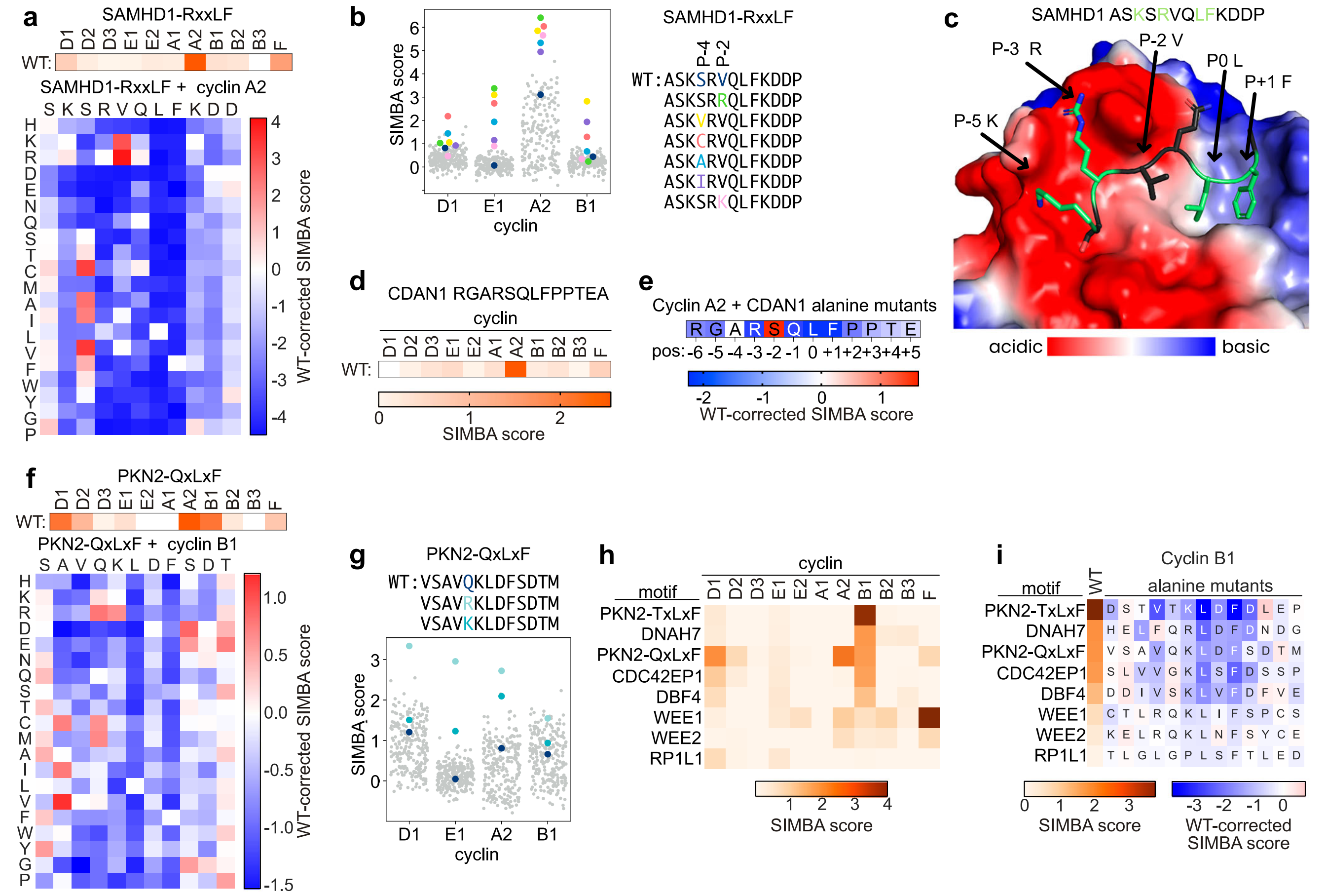

Fig. 6 | Atypical RxL-like cyclin binding motifs lacking P-2 basic residue. **a** SIMBA scores of SAMHD1 peptide for each cyclin (top) and the peptide DMS results for cyclin A2 (bottom). **b** SIMBA scores of SAMHD1 motif DMS peptides. **c** Cryo-EM structure of the SAMHD1 peptide bound to cyclin A2 hydrophobic patch, colored by electrostatic potential. **d** SIMBA scores of CDAN1 peptide. **e** Alanine-scanning of the CDAN1 peptide. Cell colors represent the wild-type subtracted score of each alanine mutant with cyclin A2. **f** SIMBA scores of PKN2-QxLxF peptide (top) and the peptide DMS results with cyclin B1 (bottom). **g** SIMBA scores of PKN2-QxLxF motif DMS peptides. **h** The cyclin specificity of LxF-type motifs in SIMBA. **i** Alanine-scanning of LxF-type peptides in SIMBA with cyclin B1. Residue shading denotes wild-type-corrected scores for Ala at each position. The leftmost column shows wild-type peptide scores. Source data are provided in Supplementary Data 4 and 5.

residue (Fig. 6e). Thus, there are multiple instances of this alternative cyclin binding mode.

Several other atypical peptides were discovered that have an LxF motif but lack a basic residue at P-2, such as the QxLxF (VSAVQKLDFSDTM) and TxLxF (SDSTVTKLDFDL) peptides from PKN2 (Supplementary Figs. 1b, c, 2e). DMS of the PKN2 QxLxF peptide revealed that cyclin B1 binding requires the LxF residues along with strong contributions from P-4 to P-1 (Fig. 6f). As with the SAMHD1 motif, binding of cyclin B1 to the QxLxF motif was improved by replacing P-2 with Arg to create an RxLxF motif, but Cys and Met also strengthened binding to a similar degree. Notably, cyclin E1 did not bind the native QxLxF peptide but it bound strongly to the RxLxF derivative (Fig. 6g). Due to higher tolerance for the lack of a basic residue at P-2 by cyclins A2 and B1 than by cyclin E1, the identity of the P-2 residue could function as a specificity filter to discriminate early and late phosphorylation in the cell cycle. We investigated six additional LxF-type peptides identified in SIMBA or phage display screens and found that three of them (from CDC42EP1, DBF4, and DNAH7) bound cyclin B1 specifically (Fig. 6h). Alanine scanning of these peptides confirmed the essential role of the LxF sequence and revealed the importance of Val at P-3 for binding cyclin B1 (Fig. 6i), which it also prefers in typical RxL motifs (Fig. 4a), as well as the role of P-4 Leu in hindering cyclin A2 binding (Supplementary Fig. 6i).

Atypical motifs with alternative hydrophobic core residues

A final category of atypical motifs was revealed by DMS results showing that the core hydrophobic Φ_0 and Φ_C positions can tolerate atypical residues (Fig. 3b, Supplementary Figs. 3d, 4a, Supplementary Fig. 5a). Surprisingly, at Φ_C, Trp and Tyr were generally favored over the consensus Leu (Fig. 7a, Supplementary Fig. 7a). The tiled library screen identified natural RxLY and RxLxY motifs in KIF20 and SGO1, respectively, as cyclin-binding peptides (Fig. 2e), and alanine scanning of the SGO1 motif confirmed the Φ_C Tyr as part of an atypical type 2 motif (Fig. 3a). At Φ_0, Ile was weaker than the predominant Leu but was frequently tolerated, especially in the context of strong motifs such as SCAPER (Fig. 7b, Supplementary Figs. 6b, 7b, c). A cryo-EM structure showed that the SCAPER variant with Ile at P0 binds cyclin A2 similarly to typical RxL peptides, with the Ile residue in the pocket usually occupied by Leu (Fig. 7c). While one RxI motif has been previously validated to bind cyclin F[44], none of the natural docking motifs found previously for CDK-binding cyclins is an RxI. An in silico search for RxIxF motifs with optimal non-core residues identified an AKRRIVF peptide in DOT1L, a Cdk2 substrate[45]. This peptide bound cyclins A2 and F (Fig. 7d), and alanine scanning confirmed the importance of the RxIxF core residues (Fig. 7e). Thus, RxI motifs provide an additional class of potential docking sites in CDK substrates.

Collectively, these data indicate that the hydrophobic patch in human cyclins recognizes a greater variety of peptides than just typical

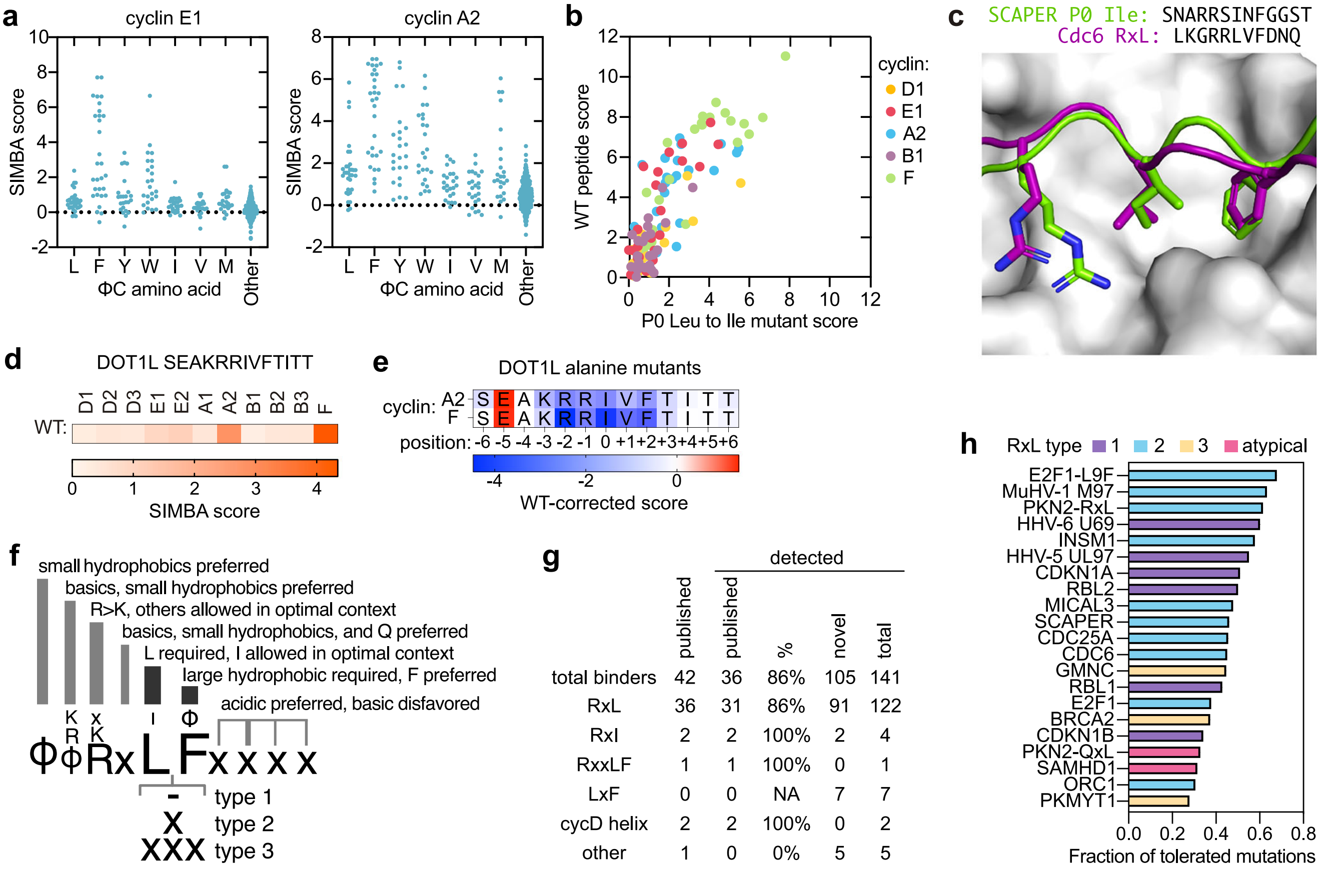

Fig. 7 | Motifs with atypical residues at core hydrophobic positions. a SIMBA scores of RxL peptides from DMS experiments with various residues at Φ_C. **b** SIMBA scores of wild-type peptides and their mutants harboring Ile at P0. **c** Cryo-EM structure showing SCAPER P0-Ile mutant peptide binding the cyclin A2 hydrophobic patch. **d** Cyclin specificity of DOT1L RxIxF peptide in SIMBA. **e** Alanine-scanning results of DOT1L RxIxF motif. The color of each cell reflects the wild-type-corrected SIMBA score of that position alanine mutant. **f** Summary of positional preferences of cyclin hydrophobic patch docking motifs. **g** Summary of cyclin binding motifs identified for all 11 cyclins tested by SIMBA. **h** The fraction of tolerated mutations, defined as mutations with a SIMBA score at least 75% of the wild-type peptide, from DMS data with cyclin A2. Source data are provided as a Source Data file and in Supplementary Data 6.

RxL motifs (Fig. 7f), as has been observed with yeast cyclins[24–26]. Furthermore, in vitro assays showed that the atypical motifs can bind cyclins with affinities in a similar range as RxL peptides (Supplementary Fig. 2b, 6b). These findings further highlight the limitations of the previous RxL consensus, as it excludes some binding variants. Nevertheless, most cyclin binding peptides match the classical RxL consensus (Fig. 7g, Supplementary Data 6). Their predominance may reflect their greater sequence tolerance in non-core positions (Fig. 7h), which could influence their likelihood of emergence during evolution.

Cyclin docking specificity in the cell cycle

The cyclin-binding peptides display varied patterns of cyclin specificity that likely relate to their functional roles. Among the 90 natural peptides that bind the major cell cycle cyclins (D1, E1, A2, B1), the majority interacted exclusively with only a single type: 35 with cyclin A2, 10 with D1, 8 with B1, and 1 with E1 (Fig. 8a, b). Cyclin A2 bound most of the cyclin E1 binding peptides, whereas the converse was not true, exposing a striking asymmetry in their overlap. Many peptides that exclusively bind cyclin A2 are from proteins involved in DNA replication, DNA repair, mitosis and chromosome segregation (Fig. 8b). Among the strong pan-cyclin motifs are proteins functioning in transcription (RBL1, RBL2, INSM1) and RxL motifs from viruses (U69, M97, UL97). Cyclin D1, the first cyclin expressed in the cell cycle, binds exclusively to Rb-like helical motifs and to a small subset of RxL motifs that are mostly also recognized by cyclin E1 (Fig. 8c, Supplementary Fig. 8a). The SIMBA data suggests that the expression of cyclin E1 brings about targeting of a wider set of RxL-containing proteins. Next, cyclin A2 binds to an even wider RxL set, possibly enabling phosphorylation of a broad spectrum of proteins, including those bound by cyclin E1 (Fig. 8c, Supplementary Fig. 8a). While cyclins E1 and A2 bind a wider set of RxL motifs than their predecessor, cyclin B1 interacts with a small subset of cyclin A2 RxLs (Fig. 8c, d, Supplementary Fig. 8a). Additionally, cyclin B1 exclusively binds several atypical RxL-like motifs and RxL motifs, such as the one from MASTL (Supplementary Fig. 5d).

Docking specificity can control phosphorylation timing

To investigate how cyclin docking motif specificity influences the temporal control of CDK substrate phosphorylation during the cell cycle, we created reporter constructs that contain five CDK phosphorylation sites (from the disordered C terminus of PKMYT1), a cyclin docking motif, a FLAG tag, GFP, and a nuclear localization signal (Fig. 8e). In pulldown experiments with these reporters, each cyclin (E, A, and B) showed a distinct pattern of docking peptide preference (Fig. 8f) that resembled those observed by SIMBA (Fig. 8e). None of the reporters captured cyclin D, potentially because cyclin D-CDK4/6 complexes are predominantly bound to p21/p27 through an extensive multipartite interface[28] in which their RxL motifs competitively occupy the hydrophobic patch. Next, we assayed phosphorylation of these reporters in synchronized human RPE1 cell cultures. We arrested cells in G1 with the Cdk4/6 inhibitor palbociclib, then released, and collected samples through the cell cycle[46] (Supplementary Fig. 8b, c). In these experiments, the different cyclins exhibited distinct and characteristic temporal expression patterns (Fig. 8g, Supplementary Fig. 8d). We used Phos-tag SDS-PAGE to monitor reporter

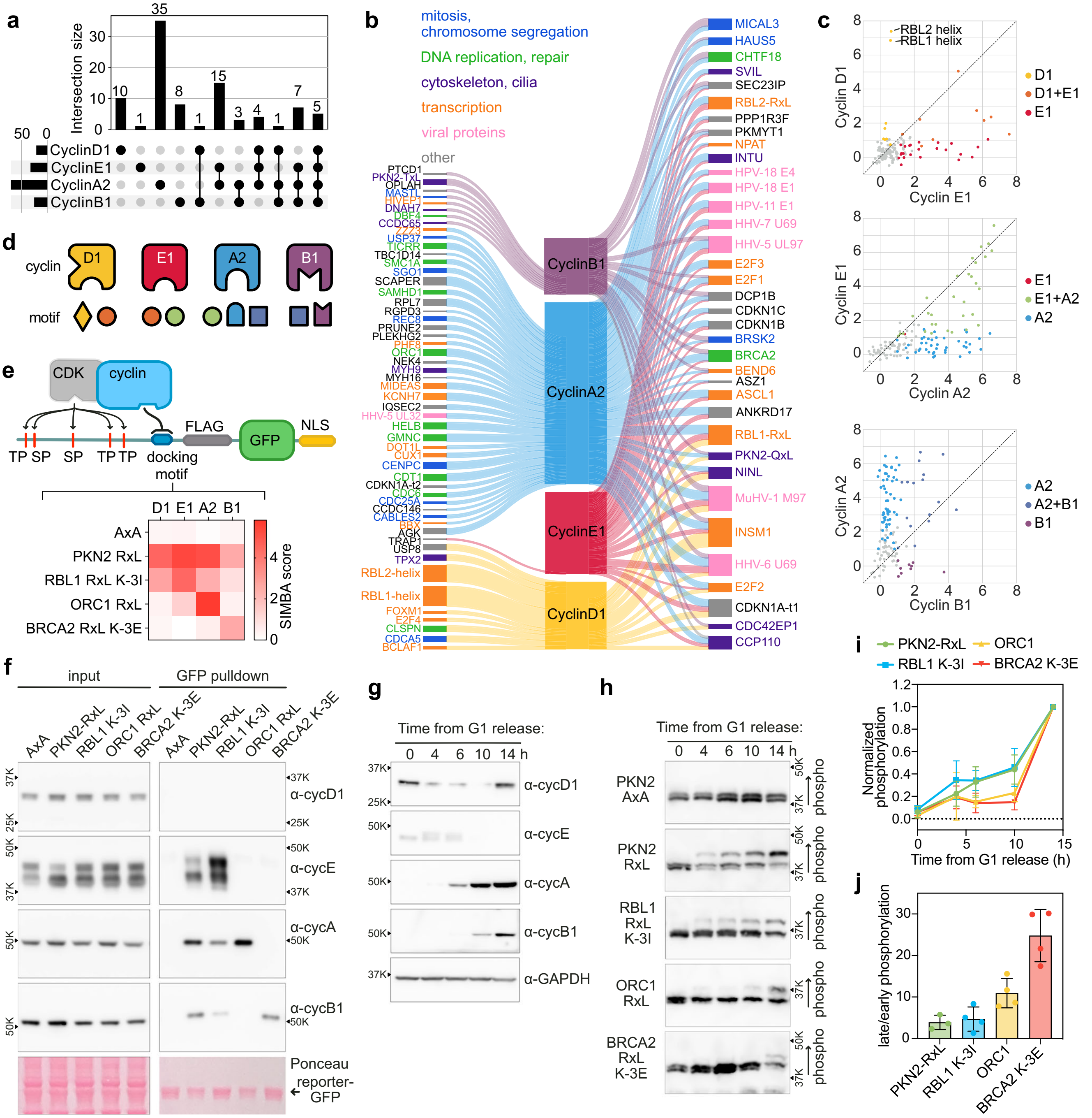

Fig. 8 | Dynamics of cyclin docking specificity in the cell cycle. a Numbers of exclusive and shared docking motifs for the major cell cycle cyclins (D1, E1, A2, B1) among wild-type peptides tested by SIMBA. Cyclin subsets lacking shared motifs (D1 + E1, E1 + B1) are not plotted. **b** Exclusive (left) and shared (right) cyclin interactors identified by SIMBA. The width of the cyclin-substrate connecting line shows the SIMBA score. Proteins are colored by UniProt keywords. **c** Comparison of wild-type peptide SIMBA scores for sequential cyclins illustrates fluctuating docking specificity during the cell cycle. **d** Schematic illustration of cyclin docking diversification. Cyclin D1 binds a small subset of RxL motifs via the hydrophobic patch and helical motifs via a different pocket, while cyclin E1 recognizes a wider set of RxL motifs. The cyclin A2 hydrophobic patch binds the largest number of peptides including more diverse RxL motifs and RxL-like motifs, whereas cyclin B interacts with a subset of RxLs and LxF-type motifs. **e** CDK activity reporter based on the C-terminal IDR of PKMYT1 fused to FLAG tag, GFP and nuclear localization signal (NLS). The heatmap shows SIMBA scores of the introduced docking motifs. **f** PKMYT1-based reporter proteins with different cyclin docking motifs were captured from human cell lysates and probed for interacting cyclins. A representative blot of two biological replicates is shown. **g** Representative western blot images showing cyclin expression in synchronized cell cultures after release from palbociclib-induced G1 arrest ($n = 2$ biological replicates). **h** The impact of docking motif specificity on phosphorylation of the PKMYT1-based reporter in palbociclib-synchronized cell cultures was monitored using Phos-tag SDS-PAGE and α-FLAG western blot. **i** Quantification of the cell cycle dependent reporter phosphorylation shown in (**h**). Each reporter is normalized to its maximum in the series. Mean ± SD; $n = 3$ (PKN2-RxL) and 4 (others) biological replicates. **j** The ratio of late (slope from 10 h to 14 h) to early (slope from 0 h to 10 h) increases in PKMYT1-based reporter phosphorylation. Mean ± SD; $n = 3$ (PKN2-RxL) and 4 (others) biological replicates. Source data are provided as a Source Data file and in Supplementary Data 6.

phosphorylation (Supplementary Fig. 8e). With the pan-cyclin RxL (PKN2-RxL), reporter phosphorylation increased gradually from 4 to 14 h after release, whereas the control motif (AxA) caused no change (Fig. 8h,i). The RBL1 K-3I RxL, which showed strong binding to cyclin E1 but reduced binding to cyclins A2 and B1, also promoted phosphorylation from 4 to 14 h, but not as strongly as the pan-cyclin RxL. (The continued increase in RBL1 K-3I reporter phosphorylation after cyclin E levels decline could be due to higher expression and activity of cyclin A2-containing CDK complexes compared to cyclin E[18].) The reporter with the cyclin A-specific ORC1 RxL showed a more abrupt increase in phosphorylation at the 14-hour time point (Fig. 8h–j). Finally, the cyclin B-specific RxL, BRCA2 K-3E, drove phosphorylation exclusively at the final time point and to a lesser extent than the stronger cyclin A docking motifs (Fig. 8h–j). As the reporter lacking cyclin docking motifs was not phosphorylated during the cell cycle, these experiments show the importance of docking interactions in determining CDK phosphorylation and demonstrate how docking motif specificity, in conjunction with gradually increasing CDK activity[18,47–49], can tune the timing of phosphorylation.

Discussion

A deep understanding of SLiM-mediated interactions requires answers to several fundamental questions. How does the sequence of a given motif-containing peptide encode specificity and affinity? How do the distinct but overlapping binding preferences of related motif-binding domains allow for the evolution of motifs that range from highly selective to promiscuous? And how accurately does a motif consensus capture the binding determinants of a motif family? In this study, we address these questions by harnessing a high-throughput, quantitative intracellular peptide binding assay to discover and characterize binding motifs for a protein family. The results provide a comprehensive analysis of SLiM-mediated recruitment of human cyclin-CDKs, quantifying the relative binding strengths of approximately 100,000 peptides to 11 cyclins spanning five families, yielding over one million measurements. This approach reveals key insights into motif-binding domain interactions that could only be uncovered through such an extensive and systematic analysis.

Through screening of tiled peptides, we identified several unreported cyclin docking motifs in human proteins, including important cell cycle regulators such as MASTL, SGO1, and GMNC. These findings demonstrate that even well-characterized SLiM families have unrecognized instances, reinforcing the idea that the census of motifs remains incomplete. Analysis of the cyclin-binding peptides revealed binding strengths differing by orders of magnitude, and specificities ranging from highly specific interactions with individual cyclins to pan-cyclin motifs capable of engaging multiple family members. In some cases, it is possible to speculate about potential physiological benefits of these differences. For example, cyclin-binding peptides from proteins that control DNA replication, such as ORC1, CDC6, and CDT1, show a strong preference for cyclin A2 over cyclin E, potentially preventing premature phosphorylation before S phase. Similarly, the cyclin B1 specific MASTL peptide could help ensure that CDK-antagonizing phosphatases are inactivated only in mitosis[39]. Conversely, strong, pan-cyclin binding by many viral motifs could reflect a strategy to outcompete host proteins, highlighting how pathogens exploit the flexibility of SLiM-mediated interactions. Variations in motif affinity might modulate the timing and/or extent of substrate phosphorylation[24,50]. For instance, submaximal binding by the E2F1 motif (compared to its RxLxF variant) may help delay E2F1 inactivation until cyclin A2 activity peaks[51]. All such effects likely act in concert with other factors such as the positioning and sequence context of phosphorylation sites, as well dynamic changes in localization, abundance, and activity of the cyclin-CDK holoenzymes[9,48,49,52]. Overall, our findings provide affinity and specificity information for many cyclin-binding motifs, allowing the development of hypotheses and raising important research questions about their biological implications for the cell cycle community to explore.

Saturation mutagenesis of cyclin docking motifs in distinct peptide contexts provides unprecedented insight into the specificity and affinity determinants of motif binding pockets. Our data uncover multiple RxL binding modes with diverse binding preferences, conformations, and surface contacts. Key findings include unequal preferences at core positions and the significant influence of non-core residues on binding. The importance of the non-core positions is exemplified by the observation that less than 15% of peptides matching the canonical RxL consensus exhibited detectable cyclin binding. Unexpectedly, we identify multiple atypical binding determinants, including a type 3 helical conformation and divergent motifs with non-canonical residues at core positions. We also noted that for all tested peptides, the affinity can be increased by mutations, validating the theory that motifs are optimized for biological output rather than for maximum binding strength. The diversity of binding determinants that modulate peptide recognition provides evolution with a broad sequence space that can be exploited to fine-tune cyclin binding from weak to strong and from highly selective to universal.

The identification of multiple binding peptides that do not conform to the consensus highlights the importance of moving beyond reliance on consensus motifs for defining binding requirements. Nevertheless, peptides matching the RxL consensus are the most frequently observed, prompting the question of why atypical variants are not more prevalent despite comparable binding affinities. Notably, they show stricter constraints at non-core positions (Fig. 7h), implying that the prevalence of the canonical consensus may be driven by the evolutionary likelihood of each binding mode. For example, type 3 RxLs are likely less common as they have more complex sequence requirements than type 1 and type 2 RxLs, and therefore are less likely to evolve ex nihilo in a protein sequence[53]. Separately, binding kinetics also play an important role in determining signaling dynamics[54] and could be a biophysical parameter driving the evolutionary selection of typical versus atypical motifs.

We note that some relevant cyclin motif interactions might still have remained undetected. First, the screens did not cover the entire proteome and therefore we would not have identified atypical motifs outside of the cell cycle proteins. Second, some weak but functional interactions could fall outside the detection limit of our method. Finally, our approach would not capture motifs that require post-translational modification, motifs encoded by peptides longer than 16 amino acids, or motifs that require cooperative interactions involving other peptide sequences or protein partners.

In conclusion, our findings provide unique insights into the sequence features encoding motif binding, deepen our understanding of how CDK outputs fluctuate during the cell cycle, and offer valuable guidance for developing therapeutic strategies targeting RxL motif-binding pockets[33]. Given the fundamental role of SLiMs in mediating protein-protein interactions, the principles uncovered here likely extend beyond cyclins, offering broader insights into the rules governing motif-based recognition. By refining our understanding of motifs, this work lays the foundation for future studies exploring the broader complexity of SLiM function, evolution, and disease relevance.

Methods

Recombinant protein purification

For fluorescence polarization experiments (FP) and peptide display, cyclins and Cdk2 were expressed in *E. coli* BL21 ArcticExpress DE3 cells (Agilent) and purified using the Ni-NTA purification system (Thermo Fisher Scientific). The 6xHis-tagged proteins were expressed from pET28a-based vectors (Supplementary Table 1). For FP, Cyclins E1 and A2 were purified as Cdk2 fusion proteins[18], while cyclin B1 and Cdk2 were purified separately and mixed subsequently. For phage display, free cyclin A2 and B1 proteins were used. The BL21 cultures were grown at 37 °C to OD600 0.4, then grown in an 11 °C shaker for 1 h, followed by IPTG addition and overnight growth at 11 °C. For cyclin B1, the cell pellets were lysed in a buffer containing 20 mM Tris-HCl pH 8.0, 800 mM NaCl, 10% glycerol, 10 mM imidazole, 0.5 mM TCEP-HCl, 1% Triton X100 supplemented with 1 mg/ml lysozyme and 1x cOmplete™ protein inhibitors cocktail (Merck). Cdk2, cyclin A2-Cdk2, and cyclin E1-Cdk2 cell pellets were lysed in 50 mM Tris-HCl pH 7.4, 500 mM NaCl, 10% glycerol, 10 mM imidazole, 0.5 mM TCEP-HCl, 0.5% Triton X-100, 1 mg/ml lysozyme and 1x cOmplete™ protein inhibitors cocktail (Merck) buffer. The His-tagged proteins were purified using Ni-NTA agarose and eluted with a buffer containing 200 mM imidazole. The eluates were then diluted 5x with 20 mM Tris-HCl pH 7.4, 300 mM NaCl, 0.1% Triton, 1 mM DTT buffer, concentrated using Amicon Ultra 4 10 K centrifugal filters, divided into small aliquots and frozen in liquid nitrogen.

Proteomic-peptide phage display (ProP-PD)

Purified cyclins were used as bait proteins in selections against the HD2 ProP-PD library containing ~950,000 overlapping 16-mer peptides from the intrinsically disordered regions of the human proteome, following the published protocol[55]. Proteins were immobilized in 96-well plates, blocked with BSA, and incubated with the ProP-PD phage library (~10^{11} phages/well). After pre-clearing with GST-coated wells, the phages were transferred to cyclin-coated wells. Following washing steps, bound phages were eluted using log-phase *E. coli* OmniMAX, amplified with M13KO7 helper phages, and grown overnight. This selection process was repeated for three additional rounds to enrich for specific binders. The enriched phage pools were then sequenced using Illumina MiSeq, and the data were analyzed with in-house Python scripts and PepTools[55]. Peptides were ranked based on occurrence in replicate selections, sequence overlap, counts, and consensus motif identification, with further focus on medium- to high-confidence peptides meeting at least three of these criteria, particularly those containing the identified motif. We performed ProP-PD to find peptides that bind to human cyclins D1, E1, A2, and B1. Cyclin D1 and E1 failed to enrich for any specific peptides, and although several cyclin-binding peptides containing RxL motifs were identified with cyclin A2 and B1 (Supplementary Fig. 1b, c), both the A2 and B1 selections were dominated by a peptide from PKN2. Surprisingly, the PKN2 peptide (VSAVQKLDFSDTMVQQ) contains a partial match to the hydrophobic part of an RxL motif (LxF) but lacks the basic residue.

Systematic intracellular motif binding analysis

Cell cycle protein peptide tiling library design. A dataset of 808 human cell cycle proteins were identified from UniProt using keywords “Cell cycle” (KW-0131), “DNA replication” (KW-0235), “Chromosome partition” (KW-0159), and “Meiosis” (KW-0469). Proteins that lacked evidence for existence at the protein level were excluded, as were proteins with extracellular, peroxisome or mitochondrial localization. AlphaFold2 structural models[56] were used to determine the intrinsically disordered regions of these proteins. Disordered residues were defined as those having less than 8 adjacent residues (residues within 6 Å of a non-hydrogen atom of each residue). This order/disorder classification was smoothened to remove short disordered or ordered regions within longer regions with the opposite classification. Regions with the annotations “Extracellular”, “Lumenal”, “Mitochondrial intermembrane”, “Perinuclear Space”, “Signal Peptide”, “Propeptide”, “Transmembrane Region”, “Intramembrane Region”, or “Initiator Methionine” were excluded, as these are inaccessible for interaction with intracellular proteins.

The accessible intracellular disordered regions of these proteins were tiled by 16-mer peptides that overlap by 14 residues. Peptides with residues that were not covered by an adjacent overlapping peptide (e.g., peptides at the beginning or end of a disordered region) were represented by two distinct synonymous oligonucleotide sequences. The final tiled set contained 91526 peptide-encoding sequences derived from 738 unique proteins. In addition to the tiled peptides, the library incorporated 60 control peptides including 24 RxL motifs, 24 inactivated RxL mutants (RxL to AxA), 3 LP motifs, 3 inactivated LP mutants (LxxP to AxxA), and 6 sequences containing STOP codons (Supplementary Data 1). Each of these 60 control peptides was represented by 4 synonymous oligonucleotide sequences.

Library design for mutational scanning. The mutational scanning was performed using 13-mer peptides containing the P0 Leu in the middle surrounded by 6 flanking N- and C-terminal residues. We performed alanine-scanning of 35 peptides and saturation mutagenesis of 25 peptides. For alanine-scanning, single alanine mutations were introduced to all positions of the 13-mer peptide. Saturation mutagenesis was carried out for either the full 13-mer or the 11-mer center region of the peptide, where variants with all 20 amino acids at each position were designed. Each peptide was encoded by three synonymous nucleotide sequences. These experiments used two distinct libraries that were tested independently. Both libraries (library 1 and library 2) included saturation mutagenesis and alanine-scanning experiments. Library 2 also included other analyses described in the text, such as comparing Arg/Lys at P-2 and Phe/Leu at Φ_C (Fig. 3f), N- and C-terminal flank swapping (Supplementary Fig. 5f, g), N-terminal contingent preferences (Fig. 5f), and scoring binding strength of previously-uncharacterized peptides that match the RxL consensus (Fig. 5c, Supplementary Fig. 5h). In addition to the experimental peptides, both libraries shared a set of 98 control peptides including 43 RxL motifs, 43 inactivated RxL mutants (RxL to AxA), 3 LP motifs, 3 inactivated LP mutants (LxxP to AxxA), and 6 sequences containing STOP codons. Each of these 98 control peptides was represented by 3 synonymous nucleotide sequences.

Cloning and yeast strains. The yeast strains used in this study are in W303 background and are listed in Supplementary Table 2. Standard methods were used for growth and genetic engineering of yeast. Yeast were grown at 30 °C in yeast extract/peptone medium with 2% glucose (YPD) or in synthetic complete medium (SC) lacking uracil (or uracil and histidine) supplemented with 2% glucose or raffinose.

The human cyclin reading frames were cloned between GST and yeast *CLN2* in the P_{GAL1}-*GST-CLN2* expression cassette (pPP4343). The intrinsically disordered N- and/or C-termini of the human cyclins were truncated to remove localization and degradation signals. To prevent the human cyclins from interacting with yeast Cdk1, a triple alanine mutation was introduced in the conserved CDK-binding interface of each cyclin (at positions corresponding to cyclin A2 residues Lys266, Glu295, and Phe304), based on prior mutations in yeast cyclins[14,57]; an exception was cyclin F, which lacks these conserved residues and does not bind CDKs. The cyclin expression constructs were harbored on replicating (CEN/ARS) plasmids or were integrated at the *HIS3* locus in yeast. The cyclin docking peptides were inserted into Ste20^{Ste5PM} chimera and expressed in yeast from a low copy number plasmid with *URA3* selection. 13-mer or 16-mer peptide sequences for mutational scanning or cell cycle protein peptide tiling libraries, respectively, were flanked by GSGG flexible linker sequences in the Ste20^{Ste5PM} construct. Oligonucleotide pools encoding docking peptides were ordered from GenScript and were amplified by PCR (10 cycles) using primers that anneal to the common flanking linkers and include MluI and SphI restriction sites. The PCR products were digested with MluI and SphI, treated with calf intestinal phosphatase, and then ligated into the MluI/SphI-digested Ste20^{Ste5PM} expression vector (pPP4745). The ligation products were transformed into *E. coli* (XL-10 Gold Ultracompetent Cells; Agilent/Agilent Technologies) and plated on LB+Amp plates. To obtain a good representation of the designed library, at least 30-fold greater number of bacterial transformants compared to the number of variants in the library were harvested and used for plasmid preparation from the pool of colonies. The plasmids used in this study are listed in Supplementary Table 1.

β-galactosidase expression assays. As a low-throughput quantitative readout of cyclin binding to the Ste20^{Ste5PM} protein, mating pathway signaling was measured in yeast strains that contain a *FUS1-lacZ* transcriptional reporter construct driving β-galactosidase expression[58]. For this, yeast cultures were grown in SC medium containing raffinose and, at OD_{600} 0.7, the exogenous cyclin expression was induced by adding galactose (2% final). After 90 min, mating signaling was activated by adding α-factor to 50 nM and the cultures were grown for an additional 45 min. Then, the yeast cells were pelleted and resuspended in 60 mM disodium phosphate, 40 mM monosodium phosphate, 10 mM KCl and 1 mM magnesium sulfate buffer. The cells were permeabilized by addition of chloroform (to 10%) and sodium dodecyl sulfate (to 0.008%), and then ortho-nitrophenyl-β-galactoside was added (to 0.9 mg/ml) as a spectrophotometric substrate for β-galactosidase activity. The reactions were incubated at 30 °C. β-galactosidase activity was estimated by measuring formation of ortho-nitrophenol in the reaction supernatant at OD_{420}.

Yeast competitive growth experiments. The pooled Ste20^{Ste5PM}-peptide expression plasmid libraries were transformed into yeast strains harboring integrated expression cassettes for different HsCyclin-Cln2 fusions. The transformation mixture was plated on SC medium plates lacking uracil, and grown at 30 °C for three days. A dilution series from the transformation was used for colony counting to ensure that the number of yeast transformants exceeds the number of peptides in the library at least 10-fold. The transformed cells were collected from the plates, diluted to 50 ml SC-URA containing raffinose and grown at 30 °C for 4–8 h. Then, the 50 ml cultures were diluted to OD_{660} 0.05 and grown overnight. At OD 0.8–1, HsCyclin-Cln2 expression was induced by adding 2% galactose. After 75 min, 40 ml of the culture (~3×10^8 cells) was collected by centrifugation and flash frozen in liquid nitrogen to obtain the t0 sample. At the same time, α-factor at 500 nM final concentration was added to the culture to begin the competitive growth experiment. The cultures were grown at 30 °C and diluted every 12 h to keep the OD_{660} below 1. Aliquots (20 ml; ~3×10^8 cells) were harvested at 20 and 32 h from α-factor addition. The harvested cells were centrifuged, washed with water, moved to 1.5 ml tubes, where the cells were pelleted by centrifugation, the cell pellets were frozen and stored at −80 °C.

Sample preparation for deep sequencing

DNA was purified from yeast cells using the Zymo Research ZR Plasmid Miniprep Kit (#D4015). Frozen cell pellets were thawed and suspended in 200 µl of solution P1, and then were lysed using Zymolyase (0.2 units/µl; Zymo Research #E1005) for 1.5 h at 37 °C, before proceeding with the remaining purification steps. Samples of plasmid DNA (4 µl) were subjected to PCR (17 cycles, 50 µl total volume) with primers that include standard P5 and P7 sequences for binding to Illumina flow cells during next generation sequencing (Supplementary Table 3). The forward primer included a P5 sequence followed by an Illumina sequencing primer binding site, a 6-nucleotide bar code, and an upstream plasmid-annealing sequence; the reverse primer included a P7 sequence followed by a 6-nucleotide i7-index sequence, an i7 sequencing primer binding site, and a downstream plasmid-annealing sequence.

Aliquots (5 µl) of the PCR products were run in 1.2% agarose gels to confirm the presence of the desired product, and the remainders were purified using Zymo Spin I columns (Zymo Research #C1003-250) and eluted in 10 mM Tris-HCl, pH 8. The concentration of the eluted products was measured using nanodrop, and a mixture was prepared containing equal amounts of each DNA product. The PCR amplicon libraries were sequenced at Novogene.

Sequencing data analysis

2FAST2Q was used to obtain the counts of different peptide-encoding oligonucleotide sequences from the deep sequencing data[59]. To calculate enrichment scores, custom Python scripts were used for the following data processing. (1) Oligonucleotides with <40 reads at t0 were dropped from further analysis. (2) The frequency of each oligonucleotide within a sample at t0, t20 and t32 was calculated. (3) The log2 fold change of t20 and t32 frequencies from the t0 frequency was calculated. (4) The log2 fold change values were z-normalized within each sample. For mutational scanning library experiments, z-normalization used the mean and standard deviation of the P0 Leu mutants; for tiled library experiments, z-normalization used the mean and standard deviation of the entire oligonucleotide population. (5) A quadratic regression (specifically, a degree 2 polynomial fit performed using numpy.polyfit) was used to correct for nonlinearity between z-scores in HsCyclin-Cln2 strains versus the unfused Cln2 strain. These corrected values are called enrichment scores. For mutational scanning libraries, this regression was performed using data from mutant RxL and LP peptides, wild-type LP peptides and STOP codon containing variants; for the tiled library, the full data set was used. (6) For each oligonucleotide, the score in the unfused Cln2 strain was subtracted from the HsCyclin-Cln2 strain score to obtain the final SIMBA score. The z-normalization and nonlinearity corrections were performed differently for data from the peptide tiling and mutational scanning experiments because in the tiling library the vast majority of variants are non-binders and thus are comparable between unfused Cln2 and HsCyclin-Cln2 strains (Fig. 1j), whereas the mutational scanning libraries contain a large fraction of HsCyclin binding peptides. Therefore, the z-normalization and nonlinearity correction of the mutational scanning experiment data was performed using the control set variants that are expected to score identically in unfused Cln2 and HsCyclin-Cln2 strains (wild-type LP, mutant LP and mutant RxL peptides, and STOP codon containing variants). As described above, we created two distinct mutational scanning libraries that were tested in independent experiments. To compare SIMBA scores for peptides in the different libraries, we used all peptides shared between the two libraries (199 total) to determine correction factors that were used to adjust the scores from library 1 to fit those in library 2. The equations used for these corrections are provided in Supplementary Data 4.

In mutational scanning experiments, each peptide is represented by 3 synonymous oligonucleotides, and the plotted data represent the median score for these 3 synonyms from two replicate experiments. Independent t-tests were performed using the set of 6 scores (3 synonyms in 2 replicates) to test if the median peptide score is greater in a given HsCyclin-Cln2 strain than in the unfused Cln2 and no cyclin strains. In the tiled library screens, each peptide is encoded by a single oligonucleotide, but adjacent 16-mer peptides overlap by 14 residues. With this library, the statistical tests were performed on sets of three consecutive peptides that group a given peptide with its preceding and subsequent peptides; these statistical tests were not performed for cyclin strains that were tested in only one replicate with the tiled library (A1, B2, B3, E2, D2, D3). The plotted data (Fig. 2b, c, e) show smoothened results that represent the rolling medians of each set of 3 consecutive peptides. The p-values from the two t-tests (i.e., HsCyclin vs. unfused Cln2 and HsCyclin vs. no cyclin) were combined using Pearson's method. Binders were defined as those with a SIMBA score >1 and Pearson's $p < 6.36 \times 10^{-6}$ or $< 5.52 \times 10^{-7}$ for mutational scanning and tiled library screening, respectively (these correspond to $p < 0.05$ after Bonferroni correction for library size). In addition, binder peptides from the tiled library screen that had a Pearson's $p < 1 \times 10^{-10}$ were designated as "high confidence" binders. While the tiled library included an additional set of (untiled) RxL control peptides, only the tiled peptides were included in Fig. 2a and Supplementary Data 2 as identified cyclin binders. Finally, to obtain a consolidated list of cyclin binding motifs detected in the tiled library screen, overlapping binding peptides were collapsed to the minimal shared sequence. Then, the SIMBA score and Pearson's p-value of the shared motif were calculated as the median of values from the individual overlapping binding peptides.

To create logos of sequence preferences, SIMBA scores were transformed into a preference PSSM as described previously[50]. First, the score for each amino acid variant was normalized to the lowest and highest scores in a given motif array. Then, these normalized scores were converted to a frequency metric by dividing each by the sum of all scores at the same position. Finally, the frequency metric was converted to a preference metric by subtracting 0.05, so that a neutral preference is represented by zero, favored residues are positive, and disfavored residues are negative. These preference scores were used to generate sequence logos via a web-based tool (http://slim.icr.ac.uk/visualisation/index.html). To compare predicted versus observed binding strength, SIMBA scores were normalized as described above and then transformed into a difference PSSM[50] by subtracting the average normalized score of all residues at a given position from the value of each residue at that position: (difference score) = (residue score) − (position average). Then, to obtain a prediction for a given peptide, the corresponding PSSM values for each residue at each position was summed across all motif positions to calculate the predicted score (PSSM sum).

Fluorescence polarization

Unlabeled peptides and N-terminally FITC-Ahx labeled PKN2-RxL peptide (SAVRKLDFSD) with >95% purity were ordered from GenScript. Fluorescence polarization was measured in a buffer containing 25 mM Hepes-KOH pH 7.4, 150 mM NaCl, 5 mM DTT and 0.05% CHAPS. The assays were carried out in black, low volume, non-binding, 384-well plates (4514, Corning). After mixing, the reactions were incubated at 37 °C in the dark for 30 min before measuring fluorescence polarization using PHERAstar FSX microplate reader. Peptide binding affinities were measured by dosing unlabeled peptides that compete with the FITC-PKN2-RxL peptide for binding to the cyclin hydrophobic patch. The optimal concentration of cyclin proteins in the experiment that allows sufficient resolution in fluorescence polarization was determined by measuring the binding affinity of the cyclins to FITC-PKN2-RxL peptide, which was 0.78 μM for cyclin A2-Cdk2, 0.17 μM for cyclin E1-Cdk2, and 3 μM for cyclin B1-Cdk2. In the competitive binding experiments, recombinant cyclin B1 was mixed at equimolar ratio with Cdk2 and used at 4 μM concentration, cyclin A2-Cdk2 was used at 0.5 μM, and cyclin E1-Cdk2 at 0.15 μM. The fluorescence polarization experiments were performed in at least two replicates. The data was analyzed and plotted using Prism 10 (Graphpad).

Generating CDK reporter expression cell lines

CDK activity reporters based on the intrinsically disordered C terminus of PKMYT1, where the native RxL motif[41] was replaced with different cyclin docking motifs. The CDK reporters were fused to a 3x FLAG tag, EGFP, and a nuclear localization signal, and expressed from a doxycycline-inducible lentiviral vector (pCW57.1). The virus was produced as follows: 7×10^5 HEK293T/17 cells (ATCC: CRL-11268) were seeded to 6-well plate and in 24 h were transfected using lipofectamine 3000 (Thermo Fisher Scientific) with psPax2 and pMD2G as packaging plasmids. 6 h after the transfection, the medium was replaced with 3 ml fresh DMEM. The medium containing the virus was collected 2 days after transfection and was used to transduce RPE1-FRT cells. RPE1-FRT cell line was obtained from Jonathon Pines (The Institute of Cancer Research, London, UK). Both HEK293T/17 and RPE1-FRT cell lines were authenticated by morphological analysis and were tested negative for Mycoplasma by qPCR at the Cancer Research UK Cambridge Institute Research Instrumentation and Cell Services core facility.

RPE1-FRT cells were cultured in high glucose DMEM supplemented with 110 mg/l pyruvate, 3.7 g/l sodium bicarbonate, and 10% fetal bovine serum in a 37 °C incubator with 5% CO_2. 24 h before transduction, 2×10^5 RPE1-FRT cells were seeded to a 6-well plate. For transduction, the medium of RPE1-FRT cells was replaced with the lentiviral supernatant and supplemented with 8 μg/ml polybrene, followed by culturing the cells for 2 days. Then, the transduced RPE1-FRT cells were collected by trypsinizing and seeded to a 6 cm dish in DMEM supplemented with 1 μg/ml puromycin. Prior to seeding for experiments, the transduced RPE1-FRT cells were split at least 3 times and cultured in the presence of puromycin to allow selection of the transduced cells.

RPE1 cell cycle synchronization

For cell cycle synchronization, 2.5×10^5 RPE1-FRT cells containing the CDK reporter expression cassettes were seeded to 10 cm dishes and grown for 32 h. Then, the medium was replaced with DMEM containing 150 nM palbociclib (Selleck Chem) to arrest cells in G1 phase and 1 μg/ml doxycycline to induce the expression of CDK reporters. The cultures were incubated at 37 °C for 24 h, after which the palbociclib-containing medium was removed, the cells were washed 3 times with 10 ml DMEM and the cells were grown in DMEM supplemented with 1 μg/ml doxycycline at 37 °C. At 0, 4, 6, 10 and 14 h, the cells were collected by trypsinization, washed with Tris buffered saline and flash frozen for immunoblotting. For propidium iodide staining, the cells were fixed with 70% ethanol and stored at −20 °C.

Propidium iodide staining and flow cytometry

The ethanol-fixed cells were washed twice with PBS and resuspended in 300 μl solution containing 5 μg/ml propidium iodide and 25 μg/ml RNase A in PBS. The mixture was incubated at 37 °C in the dark for 30 min and analyzed by flow cytometry using BD LSR Fortessa. Data from at least 10,000 cells was collected and analyzed using FlowJo (BD Biosciences).

Co-immunoprecipitation

For CDK reporter co-immunoprecipitation experiments, the RPE1-FRT-based cell lines were seeded to 15 cm dishes in DMEM, at 40% confluency, 1 μg/ml doxycycline was added to the medium to induce the reporter expression and the cells were collected and frozen at 80% confluency 24 h after induction.

The cells were lysed in buffer containing 10 mM Tris-HCl pH 7.4, 150 mM NaCl, 0.1% NP-40, 5 mM EDTA, 1 mM DTT and cOmplete™ protein inhibitors cocktail (Merck). The total protein concentration in the lysate was measured using Pierce™ Bradford Plus Protein Assay Reagent (Thermo Fisher Scientific). The lysates were diluted to 2 mg/ml total protein. For co-immunoprecipitation, 500 μg of cell lysate was mixed with 10 μl ChromoTek GFP-Trap® Magnetic Agarose beads (Proteintech) that had been equilibrated with the lysis buffer. The mixture was incubated on a rotator at 4 °C for 1 h. Then, the GFP-trap magnetic beads were collected using a magnet, the lysate was removed and the beads were washed three times with 500 μl lysis buffer. The immunoprecipitated proteins were eluted using Laemmli SDS-PAGE sample buffer and were subjected to SDS-PAGE and immunoblotting.

Immunoblotting

To analyze the phosphorylation of the CDK reporters in the cell cycle, the synchronized RPE1-FRT cells expressing the reporter-GFP fusion proteins were lysed in a buffer containing 10 mM Tris-HCl pH 7.4, 150 mM NaCl, 1% Triton X100, phosSTOP phosphatase inhibitor cocktail (Roche) and cOmplete EDTA-free protease inhibitor cocktail (Merck). The lysate was cleared by centrifugation and the total protein concentration was measured using Pierce™ Bradford Plus Protein Assay Reagent. For immunoblotting, 20 μg of cell lysate was resolved using Phos-tag SDS-PAGE with gels containing 8% acrylamide, 25 μM Phos-tag (Alpha Laboratories) and 50 μM $MnCl_2$[60]. Following electrophoresis, the gels were washed twice with 10 mM

EDTA. The proteins were transferred to nitrocellulose membrane using iBlot 2 (Thermo Fisher Scientific). After transfer, the membrane was blocked using 5% fat-free milk solution in TBS-T, followed by overnight incubation at 4 °C with the primary antibody solutions. The following primary antibodies were used: anti-cyclin D1 Antibody (DCS-6) sc-20044 (Santa Cruz Biotechnologies) at 1:500, anti-cyclin E Antibody (HE12) sc-247 (Santa Cruz Biotechnologies) at 1:500, anti-cyclin A Antibody (B-8) sc-271682 (Santa Cruz Biotechnologies) at 1:500, anti-CCNB1/cyclin B1 Antibody (GNS1) sc-245 (Santa Cruz Biotechnologies) at 1:500, anti-GAPDH (D16H11) XP® Rabbit mAb #5174 (Cell Signaling Technologies) at 1:1000, anti-FLAG tag (D6W5B) Rabbit mAb (Cell Signaling Technologies) at 1:1000. Then, the membrane was washed 5 times with TBS-T, incubated with secondary antibody solutions for 1 h, and washed again 5 times with TBS-T. HRP-conjugated anti-mouse IgG (#7076, Cell Signaling Technologies) at 1:2000 and HRP-conjugated anti-rabbit IgG (#7074, Cell Signaling Technologies) at 1:10,000 were used as secondary antibodies. The antibodies were detected using SuperSignal™ West Pico PLUS Pico Chemiluminescent substrate (Thermo Fisher Scientific).

To validate the protein bands observed in Phos-tag SDS-PAGE, lysates from asynchronous RPE1-FRT cultures expressing the CDK reporter proteins were dephosphorylated using lambda protein phosphatase. For this, 20 μg of the lysates prepared without phosphatase inhibitors were supplemented with 1 mM $MnCl_2$, 1x NEB PMP buffer and 8 U/μl lambda protein phosphatase (New England Biolabs). The reactions were incubated at 30 °C for 30 min and stopped by addition of Laemmli SDS-PAGE sample buffer. Western blot signal intensities were quantified in Image Lab (BioRad).

To assess expression of HsCyclin-Cln2 fusions, yeast cultures were grown in SC + raffinose medium and cyclin expression was induced by adding 2% galactose for 120 min. Then, 2 ml samples were harvested by centrifugation and frozen in liquid nitrogen. Frozen cells were resuspended in 300 μl TCA buffer (10 mM Tris-HCl, pH 8.0, 10% trichloroacetic acid, 25 mM ammonium acetate, 1 mM Na_2EDTA), incubated on ice for 10 min, and microcentrifuged for 10 min at 4 °C. The pellet was resuspended in 75 μl Resuspension Buffer (0.1 M Tris.HCl, pH 11.0, 3% SDS), boiled for 5 min, cooled at room temperature for 5 min, then re-centrifuged for 30 s. The supernatant (60 μl) was transferred to a new tube, 10 μl was reserved to assay protein concentration, and then 50 μl of 2x SDS Sample Buffer was added to the remainder. Total protein concentrations were measured by BCA assay (Pierce #23225), and 20 μg was loaded per lane. Proteins were resolved by SDS-PAGE, transferred to PVDF, and probed with mouse anti-GST (1:1000, Santa Cruz Biotechnologies #sc-138) or rabbit anti-G6PDH (1:100000, Sigma #A9521). HRP-conjugated secondary antibodies were goat anti-mouse (1:3000, BioRad #170-6516) or goat anti-rabbit (1:3000, Jackson ImmunoResearch #111-035-144). Chemiluminescent detection used a BioRad Clarity reagent (#170-5060) and an Amersham ImageQuant 800 instrument.

CDK2-cyclin A expression and purification for cryo-electron microscopy

Cdk2 and cyclin A were expressed separately and combined later during purification. The human Cdk2 construct (residues 1-282) was provided by John Chodera, Nicholas Levinson and Markus Seeliger (Addgene plasmid #79726; http://n2t.net/addgene:79726; RRID: Addgene_79726)[61]. Human cyclin A2 containing an N-terminal 6xHis-tag was cloned into a vector suitable for bacterial expression. For each construct, 10 ml of LB supplemented with 100 μg/ml ampicillin and 34 μg/ml chloramphenicol were inoculated with a single colony of transformed *E. coli* Rosetta (DE3) pLysS cells and incubated at 37 °C overnight. The whole overnight culture was used to inoculate 3 l of LB supplemented with 100 μg/ml ampicillin and 34 μg/ml chloramphenicol that were incubated at 37 °C. Cultures were induced at OD ~ 0.6 with 1 mM IPTG and incubated at 24 °C overnight for protein expression. Cultures were harvested by centrifugation at 10,000 × *g* for 10 min at 4 °C. Pellets were snap frozen in liquid nitrogen and stored at −80 °C.

To form the cyclin A-Cdk2 complex, 7.8 g of Cdk2 pellet and 9.5 g of cyclin A pellet were combined and resuspended in purification buffer (50 mM HEPES pH 7.5, 180 mM NaCl, 5% (v/v) glycerol, 2 mM $MgCl_2$, 2 mM DTT) supplemented with protease inhibitors and DNAseI. Cells were then lysed by sonication and the lysate was clarified by centrifugation at 20,000 *g* for 30 min at 4 °C, before spinning the supernatant for a further 15 min. The clarified lysate was supplemented with 10 mM imidazole and then loaded onto an equilibrated 5 ml HisTrap column (Cytiva). The column was washed with purification buffer supplemented with 20 mM imidazole. Complexes were eluted using a linear gradient of 20–300 mM imidazole across 60 ml, then the column was washed with purification buffer supplemented with 300 mM imidazole for a further ~30 ml. Fractions containing cyclin A-Cdk2 complexes were combined and incubated overnight with TEV protease to cleave the tags. After cleavage, complexes were buffer exchanged to gel filtration buffer (20 mM HEPES pH 7.5, 150 mM NaCl, 5 % v/v glycerol, 2 mM $MgCl_2$, 2 mM DTT), centrifuged at 3000 × *g* for 15 min at 4 °C, and then incubated with equilibrated Ni-NTA Superflow beads (Qiagen) at room temperature for 30 min to remove His6-tagged TEV protease. The flow-through was then concentrated, flash frozen in liquid nitrogen and stored at −80 °C. Complexes were thawed and further purified by gel-filtration using a Superdex 200 Increase 10/300 column (Cytiva). Cyclin A-Cdk2-containing fractions with a concentration of 2 mg/ml (1 Abs = 1 mg/ml) were aliquoted, snap frozen in liquid nitrogen and stored at −80 °C.

Cryo-EM grid preparation

Cryo-EM samples were prepared on UltrAuFoil 1.2/1.3 300 mesh holey gold grids (Quantifoil Microtools). Samples were prepared by mixing the cyclin A-Cdk2 complex (5x dilution from 2 mg/mL stock) with 300 μM of RxL peptide in cryo-EM buffer (20 mM HEPES-NaOH pH 7.5, 150 mM NaCl, 2 mM $MgCl_2$). 4 μl of each complex were applied to plasma-cleaned grids (Tergeo EM plasma Cleaner, PIE Scientific) which were blotted for 1.5–2.0 s using a Vitrobot Mark IV (Thermo Fisher Scientific) operated at 5 °C and 100% humidity, and then plunged-frozen into liquid ethane cooled by liquid nitrogen. After vitrification, grids were clipped into autogrid cartridges (Thermo Fisher Scientific) to use with autoloader systems.

Data acquisition

Grid screening and data collection were performed on a 200 kV Glacios cryo-transmission electron microscope equipped with a Falcon 4i direct electron detector (Thermo Fisher Scientific). Four grids for each complex were screened, and the best grid, as judged by ice thickness and particle distribution, was chosen for data collection. Grid squares were manually selected and automatically brought to eucentric height in EPU (Thermo Fisher Scientific), and holes were automatically detected and selected using specific relative ice thickness filters suitable for cyclin A-Cdk2 complexes. Electron micrograph movies were collected in EER format with a pixel size of 0.5675 Å/pixel, a total electron exposure of 60 $e^-/Å^2$, and a defocus range of −0.6 to −1.8 μm. In total, 6422 movies were collected for Cdk2-cyclin A-GMNC, 5078 for Cdk2-cyclin A-SAMHD1, and 4707 for Cdk2-cyclin A-SCAPER.

Image processing

For all structures, cryo-EM data were pre-processed in cryoSPARC live and cryoSPARC v4.4.1[62], and then transferred to RELION 5.0 beta[63] for further processing, 3D reconstruction, and final refinement. All refinements were done using BLUSH regularization implemented in RELION 5.0 beta[63].

In cryoSPARC live, raw EER movies were fractioned into 40 frames and motion corrected with 2x binning. The contrast transfer function

(CTF) of each motion-corrected micrograph was fitted in cryoSPARC live. Total beam-induced specimen motion, in-frame motion, relative ice-thickness, and the quality of CTF fitting were inspected to remove poor-quality micrographs, which led to 6015 micrographs being accepted for Cdk2-cyclin A-GMNC, 5078 for Cdk2-cyclin A-SAMHD1 and 4077 for Cdk2-cyclin A-SCAPER. For all three datasets, particles were picked using blob picker (circular/elliptical blob, 70–90 Å diameter) and then extracted using a box size of 160 × 160 pixels. On-the-fly 2D classification and 3D refinement using default parameters was used to assess data quality and peptide binding. Using a volume generated from the predicted structure of a Cdk2-cyclin A complex[64] using UCSF Chimera[65] as an initial reference, 447,768 particles yielded a 3.5 Å reconstruction for Cdk2-cyclin A-GMNC, 589,358 particles yielded a 3.3 Å reconstruction for Cdk2-cyclin A-SAMHD1, and 339,520 particles yielded a 3.4 Å reconstruction for Cdk2-cyclin A-SCAPER, according to Fourier Shell Correlation (FSC) at the 0.143 cut-off[66].

To maximize the selection of high-quality particles, two particle selection strategies were employed in cryoSPARC v4.4.1 for all three datasets after completion of on-the-fly processing. All blob-picked particles from the cryoSPARC live session were re-classified into 100 2D classes using a batch size of 300 particles, which resulted in 1,512,409 particles from good 2D classes retained for Cdk2-cyclin A-GMNC, 1,040,145 particles for Cdk2-cyclin A-SAMHD1, and 1,037,921 particles for Cdk2-cyclin A-SCAPER (particle set (i) identified in Supplementary Fig. 4a). Particles were also extracted using template picking using 2D averages generated by the reclassification of blob-picked particles from cryoSPARC live. Template-based picked particles were classified into 100 2D classes using a batch size of 300 particles which resulted in 1,280,980 particles from good 2D classes retained for Cdk2-cyclin A-GMNC, 916,334 particles for Cdk2-cyclin A-SAMHD1, and 869,030 particles for Cdk2-cyclin A-SCAPER (particle set (ii) identified in Supplementary Fig. 4a). Particles picked by blob-picking (particle set (i)) and template-picking (particle set (ii)) were combined with particles retained from good 2D classes from the cryoSPARC live session (particle set (iii) identified in Supplementary Fig. 4a). After removing duplicates, 2,553,964 particles were retained for Cdk2-cyclin A-GMNC, 1,712,010 for Cdk2-cyclin A-SAMHD1, and 1,741,162 for Cdk2-cyclin A-SCAPER. Retained particles were further classified into 50 2D classes using a batch size of 200 particles and duplicates were removed. After selecting good 2D classes, 1,938,556 particles were retained for Cdk2-cyclin A-GMNC, 1,473,643 for Cdk2-cyclin A-SAMHD1, and 1,446,486 for Cdk2-cyclin A-SCAPER, which were then converted to *.star files for use in RELION 5.0 beta using scripts contained in the PYEM package[67].

Motion-corrected micrographs from CryoSPARC live were imported to RELION 5.0 beta and selected particles were re-extracted using a 160 × 160 pixel box using the coordinate information from the imported particles from cryoSPARC v4.4.1. Extracted particles were subjected to masked 3D refinement. Particles were then classified into four 3D classes by 3D classification without alignment (regularization parameter $\tau = 20$). 183,712 particles for Cdk2-cyclin A-GMNC, 81,294 particles for Cdk2-cyclin A-SAMHD1, and 91,934 particles for Cdk2-cyclin A-SCAPER were selected from the best 3D class and refined to 3.6 Å resolution, 3.4 Å resolution, and 3.3 Å resolution respectively. To further improve the map quality, selected particles were subjected to CTF refinement (beam tilt and trefoil for the SAMHD1 and SCAPER datasets, and beam tilt, trefoil, and fourth-order aberrations for the GMNC dataset). For Cdk2-cyclin A-GMNC, CTF-refined particles were refined and post-processed yielding a 3.2 Å reconstruction, according to FSC at the 0.143 cut-off (Supplementary Fig. 4b). For Cdk2-cyclin A-SAMHD1 and Cdk2-cyclin A-SCAPER, CTF-refined particles were then re-refined and duplicates were removed, retaining 80,673 particles and 91,179 particles, respectively. The retained particles were then again refined and post-processed yielding a 3.1 Å reconstruction for Cdk2-cyclin A-SAMHD1 (Supplementary Fig. 6c) and a 2.9 Å reconstruction for CDK2-cyclin A-SCAPER (Supplementary Fig. 7d), according to FSC at the 0.143 cut-off.

Model building and refinement

To build the peptide-bound Cdk2-cyclin A structures an AlphaFold-predicted model[64] was fitted into each post-processed cryo-EM map (3.2 Å resolution for Cdk2-cyclin A-GMNC, 3.1 Å resolution for Cdk2-cyclin A-SAMHD1 and 2.9 Å resolution for Cdk2-cyclin A-SCAPER) using UCSF Chimera[65]. Fitted models were transferred to COOT for model building[68] and refined by real-space refinement in PHENIX[69]. Refined models were validated using MOLPROBITY[70] implemented in PHENIX. Refinement statistics for each structure are provided in Supplementary Table 4. The three-dimensional FSC of each structure was computed using the Remote 3D FSC Processing server[71].

Visualization of molecular models and creation of figures

Molecular models and cryo-EM maps were visualized in UCSF Chimera[65], UCSF Chimera X[72], and PyMOL (the PyMOL molecular graphics system, Schrödinger, LLC) for analysis, interpretation and figure preparation.

Reporting summary

Further information on research design is available in the Nature Portfolio Reporting Summary linked to this article.

Data availability

The raw data generated in this study is available in the supplementary material and at Mendeley Data (https://data.mendeley.com/datasets/bs54ny7ns2/4). Raw counts from the deep sequencing of peptide-encoding oligonucleotide sequences are provided in Supplementary Data 1 (peptide tiling SIMBA experiment) and Supplementary Data 3 (mutational scanning SIMBA experiments). The atomic models and cryo-EM maps of the and CDK2 - cyclin A2 - GMNC, CDK2 - cyclin A2 - SAMHD1 and CDK2 - cyclin A2 - SCAPER complexes have been deposited to the EM Data Resource with accession codes EMD-52201, EMD-52204, and EMD-52208 and the PDB with accession codes 9HIU, 9HIW, and 9HJ1, respectively. The previously published cyclin-CDK structures used in this study are available in the PDB under accession codes 2CCI, 1H24, 1H25, 1H26, 1H27, 1H28, 1JSU, 6P8H, 6P3W. Source data are provided with this paper.

Code availability

The python code used for data processing in this study is publicly available and has been deposited in Mendeley Data at [https://data.mendeley.com/datasets/bs54ny7ns2/4], under Apache 2.0 license.

References

1. Tompa, P., Davey, N. E., Gibson, T. J. & Babu, M. M. A million peptide motifs for the molecular biologist. *Mol. Cell* **55**, 161–169 (2014).
2. Kumar, M. et al. The eukaryotic linear motif resource: 2022 release. *Nucleic Acids Res.* **50**, D497 (2022).
3. Morgan, D. O. *The cell cycle: principles of control* (New Science Press, 2007).
4. Daub, H. et al. Kinase-selective enrichment enables quantitative phosphoproteomics of the kinome across the cell cycle. *Mol. Cell* **31**, 438–448 (2008).
5. Dephoure, N. et al. A quantitative atlas of mitotic phosphorylation. *Proc. Natl. Acad. Sci. USA* **105**, 10762–10767 (2008).
6. Errico, A., Deshmukh, K., Tanaka, Y., Pozniakovsky, A. & Hunt, T. Identification of substrates for cyclin dependent kinases. *Adv. Enzym. Regul.* **50**, 375–399 (2010).
7. Pagliuca, F. W. et al. Quantitative proteomics reveals the basis for the biochemical specificity of the cell-cycle machinery. *Mol. Cell* **43**, 406–417 (2011).

8. Matthews, H. K., Bertoli, C., Bruin, R. A. M. & de Cell cycle control in cancer. *Nat. Rev. Mol. Cell Biol.* **23**, 74–88 (2021). 2021 231.
9. Tatum, N. J. & Endicott, J. A. Chatterboxes: the structural and functional diversity of cyclins. *Semin. Cell Dev. Biol.* **107**, 4–20 (2020).
10. Schulman, B. A., Lindstrom, D. L. & Harlow, E. D. Substrate recruitment to cyclin-dependent kinase 2 by a multipurpose docking site on cyclin A. *Biochemistry* **95**, 10453–10458 (1998).
11. Wohlschlegel, J. A., Dwyer, B. T., Takeda, D. Y. & Dutta, A. Mutational analysis of the Cy motif from p21 reveals sequence degeneracy and specificity for different cyclin-dependent kinases. *Mol. Cell. Biol.* **21**, 4868–4874 (2001).
12. Lacy, E. R. et al. p27 binds cyclin–CDK complexes through a sequential mechanism involving binding-induced protein folding. *Nat. Struct. Mol. Biol.* **11**, 358–364 (2004).
13. Takeda, D. Y., Wohlschlegel, J. A. & Dutta, A. A bipartite substrate recognition motif for cyclin-dependent kinases. *J. Biol. Chem.* **276**, 1993–1997 (2001).
14. Bailly, E., Cabantous, S., Sondaz, D., Bernadac, A. & Simon, M.-N. Differential cellular localization among mitotic cyclins from Saccharomyces cerevisiae: a new role for the axial budding protein Bud3 in targeting Clb2 to the mother-bud neck. *J. Cell Sci.* **116**, 4119–4130 (2003).
15. Basu, S. et al. The hydrophobic patch directs Cyclin B to centrosomes to promote global CDK phosphorylation at mitosis. *Curr. Biol.* **30**, 883–892.e4 (2020).
16. Bentley, A. M., Normand, G., Hoyt, J. & King, R. W. Distinct sequence elements of cyclin B1 promote localization to chromatin, centrosomes, and kinetochores during mitosis. *Mol. Biol. Cell* **18**, 4847–4858 (2007).
17. Dangiolella, V. et al. SCFCyclin F controls centrosome homeostasis and mitotic fidelity via CP110 degradation. *Nature* **466**, 138–142 (2010).
18. Topacio, B. R. et al. Cyclin D-Cdk4,6 drives cell-cycle progression via the retinoblastoma Protein's C-Terminal Helix. *Mol. Cell* **74**, 758–770.e4 (2019).
19. Allan, L. A. et al. Cyclin B1 scaffolds MAD1 at the kinetochore corona to activate the mitotic checkpoint. *EMBO J.* **39**, e103180 (2020).
20. Yu, J. et al. Structural basis of human separase regulation by securin and CDK1–cyclin B1. *Nat* **2021**, 1–5 (2021).
21. Jackman, M. et al. Cyclin B1-Cdk1 facilitates MAD1 release from the nuclear pore to ensure a robust spindle checkpoint. *J. Cell Biol.* **219**, e201907082 (2020).
22. Kõivomägi, M. et al. Dynamics of Cdk1 substrate specificity during the cell cycle. *Mol. Cell* **42**, 610–623 (2011).
23. Bhaduri, S. & Pryciak, P. M. Cyclin-specific docking motifs promote phosphorylation of yeast signaling proteins by G1/S Cdk complexes. *Curr. Biol.* **21**, 1615–1623 (2011).
24. Faustova, I. et al. A new linear cyclin docking motif that mediates exclusively S-phase CDK-specific signaling. *EMBO J.* **40**, e105839 (2020).
25. Örd, M., Venta, R., Möll, K., Valk, E. & Loog, M. Cyclin-specific docking mechanisms reveal the complexity of M-CDK function in the cell cycle. *Mol. Cell* **75**, 76–89.e3 (2019).
26. Örd, M. et al. Proline-rich motifs control G2-CDK target phosphorylation and priming an anchoring protein for polo kinase localization. *Cell Rep.* **31**, 107757 (2020).
27. Cheng, K. Y. et al. The role of the phospho-CDK2/cyclin A recruitment site in substrate recognition. *J. Biol. Chem.* **281**, 23167–23179 (2006).
28. Guiley, K. Z. et al. P27 allosterically activates cyclin-dependent kinase 4 and antagonizes palbociclib inhibition. *Science* **366**, eaaw2106 (2019).
29. Lowe, E. D. et al. Specificity determinants of recruitment peptides bound to pPhospho-CDK2/Cyclin A †,‡. *Biochemistry* **41**, 15625–15634 (2002).
30. Gelais, C. S. et al. A putative cyclin-binding motif in human SAMHD1 contributes to protein phosphorylation, localization, and stability. *J. Biol. Chem.* **291**, 26332 (2016).
31. Kelso, S. et al. Bipartite binding of the N terminus of Skp2 to cyclin A. *Structure* **29**, 975–988.e5 (2021).
32. Salamina, M. et al. Discriminative SKP2 interactions with CDK-Cyclin complexes support a Cyclin A-specific role in p27KIP1 degradation. *J. Mol. Biol.* **433**, 166795 (2021).
33. Singh, S. et al. Cyclin A/B RxL macrocyclic inhibitors to treat cancers with high E2F activity. BioRxiv Prepr. Serv. Biol., 2024.08.01.605889. https://doi.org/10.1101/2024.08.01.605889 (2024).
34. Hope, I. et al. Crystallographic fragment screening of CDK2-cyclin A: FragLites map sites of protein-protein interaction. Preprint at bioRxiv, https://doi.org/10.1101/2024.06.03.596235.
35. Subbanna, M. S., Winters, M. J., Örd, M., Davey, N. E. & Pryciak, P. M. A quantitative intracellular peptide binding assay reveals recognition determinants and context dependence of short linear motifs. *J. Biol. Chem.* **301**, 108225 (2025).
36. Ferrell, J. E. Simple rules for complex processes: new lessons from the budding yeast cell cycle. *Mol. Cell* **43**, 497 (2011).
37. Enrico, T. P. et al. Cyclin F drives proliferation through SCF-dependent degradation of the retinoblastoma-like tumor suppressor p130/RBL2. *eLife* **10**, e70691 (2021).
38. Zhang, T., Liu, W. D., Saunee, N. A., Breslin, M. B. & Lan, M. S. Zinc finger transcription factor INSM1 interrupts cyclin D1 and CDK4 binding and induces cell cycle arrest. *J. Biol. Chem.* **284**, 5574 (2009).
39. Hara, M. et al. Greatwall kinase and cyclin B-Cdk1 are both critical constituents of M-phase-promoting factor. *Nat. Commun.* **3**, 1–9 (2012).
40. Balestrini, A., Cosentino, C., Errico, A., Garner, E. & Costanzo, V. GEMC1 is a TopBP1-interacting protein required for chromosomal DNA replication. *Nat. Cell Biol.* **12**, 484–491 (2010).
41. Liu, F., Rothblum-Oviatt, C., Ryan, C. E. & Piwnica-Worms, H. Overproduction of Human Myt1 kinase induces a G2 cell cycle delay by interfering with the intracellular trafficking of Cdc2-Cyclin B1 complexes. *Mol. Cell. Biol.* **19**, 5113 (1999).
42. Brown, N. R. et al. Cyclin B and Cyclin A confer different substrate recognition properties on CDK2. *Cell Cycle* **6**, 11 (2007).
43. Doig, A. J. & Baldwin, R. L. N- and C-capping preferences for all 20 amino acids in α-helical peptides. *Protein Sci.* **4**, 1325–1336 (1995).
44. D'Angiolella, V. et al. Cyclin F-mediated degradation of ribonucleotide reductase M2 controls genome integrity and DNA repair. *Cell* **149**, 1023–1034 (2012).
45. Chi, Y. et al. A novel landscape of nuclear human CDK2 substrates revealed by in situ phosphorylation. *Sci. Adv.* **6**, 9899–9916 (2020).
46. Trotter, E. W. & Hagan, I. M. Release from cell cycle arrest with Cdk4/6 inhibitors generates highly synchronized cell cycle progression in human cell culture: Cdk4/6 Induction Synchronisation. *Open Biol.* **10**, 200200 (2020).
47. Örd, M. & Loog, M. How the cell cycle clock ticks. *Mol. Biol. Cell* **30**, 169–172 (2019).
48. Gavet, O. & Pines, J. Progressive activation of CyclinB1-Cdk1 coordinates entry to mitosis. *Dev. Cell* **18**, 533–543 (2010).
49. Basu, S., Greenwood, J., Jones, A. W. & Nurse, P. Core control principles of the eukaryotic cell cycle. *Nat* **607**, 381–386 (2022).
50. Bandyopadhyay, S. et al. Comprehensive analysis of G1 Cyclin docking motif sequences that control CDK regulatory potency in vivo. *Curr. Biol.* **30**, 4454–4466.e5 (2020).

51. Dynlacht, B. D., Flores, O., Lees, J. A. & Harlow, E. Differential regulation of E2F transactivation by cyclin/cdk2 complexes. *Genes Dev.* **8**, 1772–1786 (1994).
52. Örd, M. et al. Multisite phosphorylation code of CDK. *Nat. Struct. Mol. Biol.* **26**, 649–658 (2019).
53. Davey, N. E., Cyert, M. S. & Moses, A. M. Short linear motifs – ex nihilo evolution of protein regulation. *Cell Commun. Signal. CCS* **13**, 43 (2015).
54. Corzo, J. Time, the forgotten dimension of ligand binding teaching. *Biochem. Mol. Biol. Educ.* **34**, 413–416 (2006).
55. Benz, C. et al. Proteome-scale mapping of binding sites in the unstructured regions of the human proteome. *Mol. Syst. Biol.* **18**, e10584 (2022).
56. Jumper, J. et al. Highly accurate protein structure prediction with AlphaFold. *Nat* **596**, 583–589 (2021).
57. Cross, F. R. & Jacobson, M. D. Conservation and function of a potential substrate-binding domain in the yeast Clb5 B-type cyclin. *Mol. Cell. Biol.* **20**, 4782–4790 (2000).
58. Winters, M. J. & Pryciak, P. M. Analysis of the thresholds for transcriptional activation by the yeast MAP kinases Fus3 and Kss1. *Mol. Biol. Cell* **29**, 669–682 (2018).
59. Bravo, A. M., Typas, A. & Veening, J. W. 2FAST2Q: a general-purpose sequence search and counting program for FASTQ files. *PeerJ* **10**, e14041 (2022).
60. Örd, M. & Loog, M. Detection of multisite phosphorylation of intrinsically disordered proteins using phos-tag SDS-PAGE. *Methods Mol. Biol.* **2141**, 779–792 (2020).
61. Albanese, S. K. et al. An open library of human kinase domain constructs for automated bacterial expression. *Biochemistry* **57**, 4675–4689 (2018).
62. Punjani, A., Rubinstein, J. L., Fleet, D. J. & Brubaker, M. A. cryoSPARC: algorithms for rapid unsupervised cryo-EM structure determination. *Nat. Methods* **14**, 290–296 (2017).
63. Kimanius, D. et al. Data-driven regularization lowers the size barrier of cryo-EM structure determination. *Nat. Methods* **21**, 1216–1221 (2024).
64. Abramson, J. et al. Accurate structure prediction of biomolecular interactions with AlphaFold 3. *Nature* **630**, 493–500 (2024).
65. Pettersen, E. F. et al. UCSF Chimera – A visualization system for exploratory research and analysis. *J. Comput. Chem.* **25**, 1605–1612 (2004).
66. Rosenthal, P. B. & Henderson, R. Optimal determination of particle orientation, absolute hand, and contrast loss in single-particle electron cryomicroscopy. *J. Mol. Biol.* **333**, 721–745 (2003).
67. Asarnow, D., Palovcak, E. & Cheng, Y. asarnow/pyem: UCSF pyem v0.5. Version v0.5 (Zenodo). https://doi.org/10.5281/zenodo.3576630 (2019).
68. Emsley, P., Lohkamp, B., Scott, W. G. & Cowtan, K. Features and development of Coot. *Acta Crystallogr. D. Biol. Crystallogr.* **66**, 486–501 (2010).
69. Afonine, P. V. et al. Real-space refinement in PHENIX for cryo-EM and crystallography. *Acta Crystallogr. Sect. Struct. Biol.* **74**, 531–544 (2018).
70. Williams, C. J. et al. MolProbity: more and better reference data for improved all-atom structure validation. *Protein Sci.* **27**, 293–315 (2017).
71. Tan, Y. Z. et al. Addressing preferred specimen orientation in single-particle cryo-EM through tilting. *Nat. Methods* **14**, 793–796 (2017).
72. Goddard, T. D. et al. UCSF ChimeraX: meeting modern challenges in visualization and analysis. *Protein Sci. Publ. Protein Soc.* **27**, 14–25 (2018).

Acknowledgements

We thank Martha Cyert for critical feedback on the manuscript, Chris Richardson for support with high-performance computing, Mardo Kõivomägi for sharing cyclin-CDK expression constructs, Jonathon Pines for feedback on the manuscript and sharing cyclin constructs and RPE1-hTERT cell line, and Pau Creixell and the Creixell lab for support. N.E.D. and M.O. are funded by a Cancer Research UK Senior Cancer Research Fellowship (C68484/A28159). M.O. was also funded by UKRI grant EP/X042065/1 and Boehringer Ingelheim Fonds travel grant. Work by M.J.W., M.S.S., and P.M.P. was funded by grants from the NIH to P.M.P. (R01GM057769 and R01GM145795). B.J.G. was supported by a Career Development Award from the Medical Research Council of the UK, grant MR/V009354/1. Work by J.C. and C.B. was funded by the Swedish Research Council (YI: 2020-03380).

Author contributions

M.O., P.M.P., and N.E.D. conceived and designed the work. M.O., M.J.W., M.S.S., and P.M.P. performed the SIMBA experiments. M.O. performed the FP, protein pulldown assays and phosphorylation assays. N.M.G., V.I.C., and B.J.G. performed the cryo-EM experiments. J.K. and C.B. performed the ProP-PD experiments. M.O. performed the data processing. M.O., B.J.G., Y.I., P.M.P., and N.E.D. acquired funding and supervised the experiments. M.O., P.M.P., and N.E.D. wrote the manuscript with input from all authors. All authors provided comments for the manuscript before submission.

Competing interests

The authors declare no competing interests.

Additional information

Supplementary information The online version contains supplementary material available at https://doi.org/10.1038/s41467-025-62765-z.

Correspondence and requests for materials should be addressed to Peter M. Pryciak or Norman E. Davey.

Peer review information *Nature Communications* thanks Mardo Kõivomägi, who co-reviewed with Devin BradburnMatthias Geyer, Josh Tycko and the other, anonymous, reviewer(s) for their contribution to the peer review of this work. A peer review file is available.